

DRYP 1.0: A parsimonious hydrological model of DRYland Partitioning of the water balance

Edisson A. Quichimbo¹, Michael Bliss Singer^{1,3,4}, Katerina Michaelides^{2,4,5}, Daniel E.J. Hobley¹, Rafael Rosolem^{5,6}, Mark O. Cuthbert^{1,3,7}

5 ¹School of Earth and Environmental Sciences, Cardiff University, Cardiff, CF10 3AT, UK

²School of Geographical Sciences, University of Bristol, Bristol, BS8 1SS, UK

³Water Research Institute, Cardiff University, Cardiff, CF10 3AT, UK

⁴Earth Research Institute, University of California Santa Barbara, Santa Barbara, California, USA

⁵Cabot Institute for the Environment, University of Bristol, Bristol, UK

10 ⁶University of Bristol, Faculty of Engineering, University Walk, Clifton BS8 1TR, UK

⁷ School of Civil and Environmental Engineering, The University of New South Wales, Sydney, New South Wales, Australia

Correspondence to: Edisson A. Quichimbo (quichimbomiguitamaea@cardiff.ac.uk)

Abstract. Dryland regions are characterized by water scarcity and are facing major challenges under climate change. One difficulty is anticipating how rainfall will be partitioned into evaporative losses, groundwater, soil moisture and runoff (the water balance) in the future, which has important implications for water resources and dryland ecosystems. However, in order to effectively estimate the water balance, hydrological models in drylands need to capture the key processes at the appropriate spatiotemporal scales. These include spatially restricted and temporally brief rainfall, high evaporation rates, transmission losses and focused groundwater recharge. Lack of available input and evaluation data and the high computational costs of explicit representation of ephemeral surface-groundwater interactions restrict the usefulness of most hydrological models in these environments. Therefore, here we have developed a parsimonious distributed hydrological model (DRYP) that incorporates the key processes of water partitioning in dryland regions with limited data requirements, and we tested it in the data-rich Walnut Gulch Experimental Watershed against measurements of streamflow, soil moisture and evapotranspiration. Overall, DRYP showed skill in quantifying the main components of the dryland water balance including monthly observations of streamflow (Nash efficiency (NSE) ~ 0.7), evapotranspiration (NSE > 0.6) and soil moisture (NSE ~ 0.7). The model showed that evapotranspiration consumes $> 90\%$ of the total precipitation input to the catchment, and that $< 1\%$ leaves the catchment as streamflow. Greater than 90 % of the overland flow generated in the catchment is lost through ephemeral channels as transmission losses. However, only $\sim 35\%$ of the total transmission losses percolate to the groundwater aquifer as focused groundwater recharge, whereas the rest is lost to the atmosphere as riparian evapotranspiration. Overall, DRYP is a modular, versatile and parsimonious Python-based model which can be used to anticipate and plan for climatic and anthropogenic changes to water fluxes and storage in dryland regions.

35

1. Introduction

Drylands are regions where potential evapotranspiration far exceeds precipitation and where water is scarce. Consequently, the water balance in such area is highly sensitive to climatic forcing in terms of the delivery of precipitation and the evaporative demand from the atmosphere (Goodrich et al., 1997; Kipkemoi et al., 2021; Pilgrim et al., 1988; Zoccatelli et al., 2019). A key challenge is anticipating how rainfall partitioning into evaporative losses, groundwater, soil moisture and runoff, is likely to change under a future climate. Hydrological models provide important insights into the translation of climate information to water partitioning at or below the land surface. However, drylands exhibit several key hydrological processes that are distinct from humid regions and which are typically omitted from most current hydrological models (Huang et al., 2017). The lack of simple, computationally efficient hydrological models for drylands undermines efforts to anticipate and plan for climatic and anthropogenic changes to water storage and fluxes in catchments, with implications for water resources for ecosystems and society (Huang et al., 2017). Drylands cover around 40 % of the global land surface (Cherlet et al., 2018) and support a population of around two billion people (White and Nackoney, 2003), yet there are no widely available, parsimonious models for simulating the dryland water balance. Climatically, dryland regions are characterised by high rates of evapotranspiration and low annual precipitation delivered with high spatial and

55 temporal variability (Aryal et al., 2020; Wheater et al., 2007; Zoccatelli et al., 2019). Precipitation events are characterised by high intensity and low duration rainfall over restricted spatial areas (Pilgrim et al., 1988). This results in a highly dynamic hydrological system prone to flash flooding, and also to water scarcity and food
insecurity, societal risks that are exacerbated by climate change, population growth and dryland expansion
(Cuthbert et al., 2019a; Giordano, 2009; Huang et al., 2017, 2015; Reynolds et al., 2007; Siebert et al., 2010;
Taylor et al., 2012; Wang et al., 2017).

60 In drylands, runoff occurs mainly as infiltration excess (Hortonian) overland flow due to high intense precipitation events, and it leads to the development of short-lived streamflow in ephemeral streams. These ephemeral streams play an important role in the water balance because high transmission losses of water through porous stream beds are the main source of aquifer recharge in such environments - a mechanism called focused recharge (Abdulrazzak, 1995; Coes and Pool, 2007; Cuthbert et al., 2016; Goodrich et al., 2018, 2013; Schreiner-McGraw et al., 2019; Shanafield et al., 2014). In contrast, diffuse recharge, which is the result of local infiltration of water below the
65 evaporation zone within the soil, is typically limited in drylands due to low precipitation and high rates of evapotranspiration (Schreiner-McGraw et al., 2019; Taylor et al., 2013). These conditions result in dryland environments having no significant long-term storage of water within soils (Huang et al., 2017; Pilgrim et al., 1988).

70 The complexity of rainfall regimes, runoff generation processes and subsurface flow paths in drylands create challenges for data collection, resulting in a paucity of data, and consequently it restricts the use of numerical models to enhance understanding of the water balance (Abbott et al., 1986; Cuthbert et al., 2019b; Ewen et al., 2000; Ivanov et al., 2004; Michaelides and Wainwright, 2002; Noorduijn et al., 2014; Schreiner-McGraw et al., 2019; Šimunek et al., 2006; Wheater et al., 2007; Woodward and Dawson, 2000; Woolhiser, 1989). Existing
75 hydrological models, operating at catchment to regional scales, are challenged in drylands due to their inherent assumptions about key flow processes and due to hard-coded parameterizations required to ensure convergence and numerical stability (e.g. physically-based models (Kampf and Burges, 2007)). Models also generally lack the ability to represent the development of ephemeral streams and their potential hydraulic interactions with groundwater systems (Quichimbo et al., 2020; Zimmer et al., 2020). Despite the recent improvement in models to
80 include transmission losses (e.g. Hughes et al. (2006); Hughes (2019); Lahmers et al. (2019); Mudd (2006)), availability of appropriate numerical tools that allow a better description of surface-groundwater interactions are still limited at catchment, regional and global scales. Ephemeral flow in streams and losses to the subsurface are currently underrepresented in medium to large scale models, despite representing half of the global stream network length (Datry et al., 2017). Additionally, the degree of complexity of existing models and their inherently high
85 computational cost does not allow for comprehensive sensitivity and uncertainty analysis, which would support the evaluation and interpretation of model results.

90 In this context, it is important for models to capture the linkages between the spatially and temporally variable climate, nonuniform runoff generation, soil moisture and focused groundwater recharge to support predictive capability of how the dryland water balance may shift with changes in climate. Models also need to include groundwater processes in drylands where the low regional hydraulic gradient governs the redistribution of groundwater resources, such as water availability for evapotranspiration in riparian areas (Maxwell and Condon, 2016; Mayes et al., 2020). Only a few large-scale hydrological models include gradient-based (diffuse) groundwater flow processes (de Graaf et al., 2015; Reinecke et al., 2019; Vergnes et al., 2012). These processes
95 should be kept simple to make them transferable to different catchments regardless of their scale. Useful dryland models should also be able to employ the limited information available, while being numerically efficient enough to allow for evaluation of the model performance and uncertainty.

100 Here we present the development of a parsimonious model which considers the main processes that control the water partitioning, fluxes, and changes in water storage in dryland regions for estimation of runoff, soil moisture, actual evapotranspiration and groundwater recharge. We do not intend for this model to accurately simulate event-based flood hydrographs, for example, for flood hazard analysis. Instead, we aimed to develop a model that captures the long-term behaviour of the water balance in dryland regions. Here we apply and test our new model

in the Walnut Gulch Experimental Watershed (WGEW), in SE Arizona, USA, where availability of high-resolution data enabled us to evaluate the model performance.

2. DRYP: a parsimonious model for DRYland regions water Partitioning

2.1. Model overview

The main hydrological processes that control fluxes and storage of water in dryland regions are shown in Fig. 1a. The movement of water through the different storage components within the catchment is characterised as follows: spatially distributed rainfall falling during individual events over the surface is partitioned into *infiltration* and *runoff*, depending on the temporal and spatial characteristics of the rainfall and the antecedent soil moisture conditions at the beginning of the rainfall event (Goodrich et al., 1997; Zoccatelli et al., 2019). Water infiltrated into the soil can be extracted by plant evapotranspiration and/or soil evaporation, or it can percolate to the water table as *diffuse recharge*. Runoff is routed to the nearest stream based on topographic gradient. In each stream reach, water may be added through groundwater discharge as *baseflow* or water may be lost through the porous boundaries by *transmission losses* as it moves downstream. The volumes of both baseflow and transmission losses are dependent on the water table depth (Quichimbo et al., 2020). Transmission losses into the near-channel alluvial sediments increase the water available for plant evapotranspiration in the *riparian zone* and also generate *focused recharge* when the water holding capacity of the sediments in the riparian zone is exceeded (Schreiner-McGraw et al., 2019). Groundwater discharge into streams depends on the hydraulic gradient, occurring when the water table elevation is higher than stream stage elevation. Additionally, when the water table is close to the surface, *capillary rise* increases the root zone water availability for riparian plant evapotranspiration. Finally, anthropogenic activities, such as localized stream and groundwater abstraction as well as irrigation, may affect the storage and fluxes of the water balance.

The only forcing variables in DRYP are spatially explicit fields of precipitation and potential evapotranspiration. The partitioning of the water balance then depends on the combination of this forcing and its interactions with spatially distributed parameters representing topography, land cover, soil hydraulic properties, hydrogeological characteristics of the aquifer, and anthropogenic activities (Fig. 1b). Hydrological processes in DRYP are structured into three main components: i) a surface water component (SW) where precipitation is partitioned into infiltration and overland flow, which is then routed through the model domain based on the topographic gradient; ii) an unsaturated zone (UZ) component that represents the soil and a riparian area parallel to streams; and iii) a saturated zone (SZ) component which represents groundwater flow (Fig. 1c). All three components in DRYP are discretized as square grid cells, and all components are vertically integrated into a computational one-way sequential scheme (Fig. 1c). However, all components are hydraulically interconnected, allowing for gradient-driven, and potentially bi-directional water exchange (Fig 1c and d).

Figure(1)

DRYP is written in Python and uses the Python-based Landlab package, which has versatility to handle gridded datasets and model domains (Barnhart et al., 2020; Hobley et al., 2017a). DRYP is structured in a modular way to allow user flexibility to control the desired level of process and parameter complexity, as well as the grid size and time-stepping choices appropriate for the desired application of the model. The grid size is the same for all layers, but the time step for different components may vary flexibly as described below. All grid cells potentially consist of all the process elements shown in Fig. 1d. However, the stream and riparian components can be excluded if stream channel characteristics are not provided, in which case all generated runoff in a cell will simply be routed to the next downstream cell with no additional losses or interactions. The size of the stream and riparian zone is only limited by the grid size.

For all cells, at the beginning of every time step, the input rainfall (P) is partitioned into surface runoff (RO) and infiltration (I) depending on the available water content of the unsaturated zone (UZ). Water in the UZ can be extracted as actual evapotranspiration (AET), a combination of soil evaporation and plant transpiration, and/or

155 percolate (R) to the saturated zone (SZ), depending on the water content and hydraulic properties of the unsaturated zone. If a cell is defined as a stream, transmission losses (TL) or groundwater discharge contributing to base flow (BF) and a riparian unsaturated zone (RUZ) are included in the local partitioning. The riparian zone is defined as an area parallel to the stream with a specified width. The riparian zone receives contributions from TL and a volume of infiltrated water proportional to the riparian area. Water within the riparian zone can either percolate, becoming focused recharge or it can be extracted by plants as riparian evapotranspiration. Focused and diffuse recharge are combined as the main inputs to the SZ, which may also interact with the UZ depending on the water table elevation as it rises and falls through the simulation. The movement of water in SZ is driven by the lateral hydraulic gradient. Additionally, anthropogenic interactions in the model are implemented as localized fluxes from the saturated zone (ASZ) and streams (AOF), whereas water abstraction for irrigation (AUZ) is delivered to the surface where it then contributes to infiltration into the unsaturated zone.

160 165 2.2 Model input files and parameter settings

170 DRYP requires spatial characterisation of key input parameters and data including a digital elevation model (DEM), channel properties in cells where streams are explicitly defined (length, width and saturated hydraulic conductivity), land cover (plant rooting depth), various soil hydraulic properties, and aquifer properties (specific yield, aquifer thickness, and saturated hydraulic conductivity) (Fig. 1). A summary of model parameters for the different model components and structures is presented in Table 1. If parameters are not provided, 'global' default values are used as defined in Table 1. The following sections describe in detail all implementation of each process included in DRYP.

175 Precipitation and potential evapotranspiration are the only forcing variables and can be supplied as either spatially variable gridded data sets in netCDF format or as spatially uniform values for each time step. Gridded data sets must be interpolated or aggregated to match the model grid resolution.

180 Table(1)

2.3 Surface Component

185 Two main processes are considered in the surface component: i) the partitioning of precipitation into infiltration and runoff, and ii) runoff routing and the partitioning of runoff into streamflow and transmission losses in stream cells. These are described below.

2.3.1 Infiltration and runoff

190 The partitioning of precipitation into infiltration and runoff at the land surface is a key process in drylands and a potentially major source of uncertainty in the overall water partitioning for these regions. Hence, four different infiltration approaches have been included in DRYP, which can be toggled on or off within the main control file (prior to simulation) to allow the user to experiment with different infiltration model structures. These approaches include two point-scale methods: the Philip infiltration approach and the Modified Green & Ampt method; and two upscaled methods for summarising infiltration over larger areas: the Upscaled Green & Ampt and the Multiscale Schaake approach.

Method 1: Infiltration based on Philip's equation

195 In this option, infiltration, $f[\text{L T}^{-1}]$ during a rainfall event is based on the explicit solution of the infiltrability depth of Philip's equation (Philip, 1957).

$$200 f(t_c) = \frac{1}{2} S_p t_c^{-\frac{1}{2}} + K_{sat}, \quad (1)$$

where: K_{sat} is saturated hydraulic conductivity [$L T^{-1}$], S_p is sorptivity [$L^2 T^{1/2}$], and t_c is time since the beginning of the precipitation event [T]. The sorptivity term is estimated by using the following equation (Rawls et al., 1982):

$$S_p = [2K_s(\theta_{sat} - \theta)|\psi_f|]^{\frac{1}{2}}, \quad (2)$$

where: θ is volumetric water content [$L^3 L^{-3}$], θ_{sat} is volumetric water content at saturated conditions [$L^3 L^{-3}$], and ψ_f is suction head [L] estimated as (Clapp and Hornberger, 1978):

$$|\psi_f| = \psi_a \frac{2\lambda+2.5}{\lambda+2.5}, \quad (3)$$

where: ψ_a is maximum suction head [L], and λ is a parameter that represents the pore size distribution of the soil [-] (Clapp and Hornberger, 1978).

The total infiltration depth in any given cell, I [L], during a precipitation event is estimated by solving the integral of Eq. (1) over the event duration. The integral of Eq. (1) is solved using the time compression approach (TCA) (Holtan, 1945; Mein and Larson, 1973; Sherman, 1943; Sivapalan and Milly, 1989), assuming that infiltration after ponding depends on the cumulative infiltrated volume. Therefore, to match the initial infiltration rate at the beginning of each time step with the infiltration at the end of the previous time step, the start time of infiltration is shifted to match the total cumulative infiltration. A more detailed description and the analytical solution of the approach can be found in Assouline (2013) and Chow et al. (1988).

Method 2: Infiltration based on a Modified Green - Ampt method

We have implemented a modified version of Green & Ampt approach defined by the following equation (Michaelides and Wilson, 2007; Scoging and Thornes, 1979):

$$f(t_c) = K_{sat} + \frac{B}{t_c}, \quad (4)$$

where: B represents initial suction head [L], t_c is the same as Eq. (1); here we use sorptivity (Eq. 2) as a proxy of the initial head owing to the nonlinear dependency of sorptivity on the water content of the soil.

The integral of Eq. (4) was also solved using the time compression approach (Holtan, 1945; Mein and Larson, 1973; Sherman, 1943; Sivapalan and Milly, 1989). However, since there is no explicit solution for Eq. (4), we used an implicit solution.

Method 3: Infiltration based on an Upscaled Green - Ampt method

This method is based on the semi-analytical solution of the Green and Ampt equation for spatially heterogeneous hydraulic conductivity developed by Craig et al. (2010):

$$\bar{I}(t_c) = \frac{p}{2} \operatorname{erfc} \left(\frac{\ln(pX) - \mu_Y}{\sigma_Y \sqrt{2}} \right) + \frac{1}{2X} \log|K_{sat}| \operatorname{erfc} \left(\frac{\sigma_Y}{\sqrt{2}} - \frac{\ln(pX) - \mu_Y}{\sigma_Y \sqrt{2}} \right) + p \int_0^{X(t_c)} \varepsilon(X(t), K_{sat}) f_k(K_{sat}) dK_{sat} \quad (5)$$

where: \bar{I} is the mean infiltration rate [$L T^{-1}$], p is the precipitation rate [$L T^{-1}$], t_c the same as Eq. (1), f_k is the probability density function of K_{sat} , μ_Y and σ_Y are mean and standard deviation of the log saturated hydraulic conductivity, $\mu_Y = \ln|K_{sat}| - \frac{1}{2} \sigma_Y^2$, X is a dimensionless time estimated as:

$$X = \frac{1}{1 + \frac{\alpha}{P t_c}}, \quad (6)$$

250 where: $\alpha = |\psi_f|(\theta_{sat} - \theta)$, with ψ_f representing the suction head.

The $\varepsilon(X, K_s)$ in Eq. (5) is an error function that can be estimated by the following approximation (Craig et al., 2010):

$$255 \quad \varepsilon \approx 0.3632 \cdot (1 - X)^{0.484} \cdot \left(1 - \frac{K_{sat}}{pX}\right)^{1.74} \left(\frac{K_{sat}}{pX}\right)^{0.38} \quad (7)$$

The $f_k(K_s)$ is assumed as a lognormal distribution following Craig et al. (2010):

$$260 \quad f_K(K_{sat}) = \frac{1}{K_{sat}\sigma_Y\sqrt{2\pi}} \exp\left(-\frac{(\ln(K_{sat}) - \mu_Y)^2}{2\sigma_Y^2}\right) \quad (8)$$

As suggested by Craig et al. (2010), we solve the integral of the Eq. (5) efficiently using a 2-point Gauss-Lagrange numerical integration method.

Method 4: Infiltration based on the Multi-scale Schaake method

265 The Schaake et al. (1996) approach is based on the assumption that rainfall and infiltration rates follow an exponential distribution to approximate spatial heterogeneity of soil properties. Therefore, the spatially averaged infiltration I [L] is estimated as:

$$270 \quad I = \frac{PI_c}{P+I_c}, \quad (9)$$

where: P is total rainfall [L] and I_c is cumulative infiltration capacity [L].

Infiltration capacity is estimated as (Schaake et al., 1996):

$$275 \quad I_c = (\theta_{sat} - \theta)(1 - \exp(-k_{dt})), \quad (10)$$

where k_{dt} is a constant that depends on soil hydraulic properties.

Following Chen & Dudhia (2001) we define k_{dt} as:

$$280 \quad k_{dt} = k_{dt\text{ref}} \frac{K_{sat}}{K_{ref}}, \quad (11)$$

where: K_{ref} [L T⁻¹] is a reference hydraulic saturated conductivity equal to 2×10^{-6} m s⁻¹ (Chen and Dudhia, 2001; Wood et al., 1998) and the parameter, $K_{dt\text{ref}}$, is specified as a scale calibration parameter.

285 **2.3.2 Runoff routing and transmission losses**

Rainfall that does not infiltrate (i.e. precipitation, P , minus infiltration, I) into the unsaturated component is routed over the model domain based on topography. The flow routing scheme varies depending on whether a cell is defined as a stream. A simple flow accumulation approach is used in cells without a defined stream, whereas for defined stream cells, an additional flux term is added to the flow accumulation approach to account for groundwater interactions via the riparian zone. This flux will either be a transmission loss or a baseflow contribution from the saturated component.

Flow routing in cells without streams

Runoff produced in any given cell is instantaneously routed to the next downstream cells using the flow accumulation approach implemented in Landlab (Braun and Willett, 2013; Hobley et al., 2017b).

The next runoff downstream cell is estimated using a D8 flow direction approach (8 potential directions based on adjacent cells). The flow accumulation method adds the amount of runoff from the upstream cells:

$$Q_i = \sum_{i=1}^N Q_{in_i}, \quad (12)$$

300

where: $Q_{in} [L^3]$ is the volume of water that discharges from upstream cells into the current cell i , N is the number of upstream cells discharging into the current cell, and $Q_i [L^3]$ is the volume of water in the cell.

Flow routing in stream cells

305 In defined stream cells, the amount of water entering the cell, $q_{in} [L^3 T^{-1}]$, is instantly reduced by any transmission losses, $i_{ch} [L^3 T^{-1}]$, and any remaining water, $q_{out} [L^3 T^{-1}]$, is moved to the next downstream cell:

$$q_{out} = q_{in} - i_{ch} \quad (13)$$

310 Water from the upstream cell, q_{in} , is assumed to be released to the next cell following a linear reservoir approach:

$$q_{in} = q_0 e^{-k_T t^*}, \quad (14)$$

315 where: $k_T [T^{-1}]$ is a recession term that is equal to the inverse of the residence time of the streamflow at each cell, t^* represents time [T], and q_0 is the initial flow rate of water entering the channel, estimated as:

$$q_0 = (Q_{in} + S_{SW} - Q_{ASW})k_T, \quad (15)$$

320 where: $Q_{ASW} [L^3]$ is the volume of water abstracted from the stream, and $S_{SW} [L^3]$ is water stored in the channel.

325

It is assumed that the sediments in the streambed are homogenous. In order to use an explicit approach at the same time as maintaining the simplicity of the model, the channel cross section is assumed to be rectangular. Consequently, the rate of infiltration depends on the wetted perimeter of the channel, and the infiltration rate, i_{ch} , at the stream cell is estimated assuming a unit gradient Darcian flow across the wetter perimeter:

$$i_{ch} = K_{ch} (2y + W)L_{ch} \quad (16)$$

330 where $K_{ch} [L T^{-1}]$ is saturated hydraulic conductivity of the streambed, $L_{ch} [L]$ is channel length for a given cell, W is channel width [L], and y is streamflow stage [L]. If the rate of water entering the stream cell is less than the potential channel infiltration rate, flow to the next downstream cell is set to zero (all water is lost via infiltration) and $i_{ch} = q_{in}$.

335 Stream stage, y , is estimated by assuming that flow velocity does not change along the channel in any given cell (no flow acceleration). Therefore, the streamflow stage and the volume at any time along the channel are kept constant in any given stream cell. A constant velocity approach assumes that there are no backward effects on the streamflow routing approach. Thus, the stream stage is estimated as the height of the rectangular prism with area $A = W L_{ch}$ and volume at time t as:

$$y = \frac{q_{in}}{A} \quad (17)$$

340

After substituting Eq. (17) into Eq. (16) and then into Eq. (13), the time integral of Eq. (13) represents the total amount of water, $Q_{out} [L^3]$, that moves to the next downstream channel cell (becoming Q_{in}):

$$Q_{out} = \int_0^{\min[t_{q=0}, \Delta t]} \left[q_0 e^{-k_T t} - L_{ch} K_{ch} \left(2 \frac{q_0 e^{-k_T t}}{W L_{ch}} + W \right) \right] dt \quad (18)$$

345

Note that the time step choice is important to bear in mind with respect to the size of the catchment modelled, since it represents the minimum travel time for flow to reach the catchment outlet.

350 The amount of water stored in the channel is estimated by applying a mass balance of all inputs and outputs of the channel:

$$S_{RO}^t = Q_{in} + S_{SW}^{t-1} - Q_{ASW} - Q_{TL} - Q_{out} \quad (19)$$

355 where: t represents the current time step, and Q_{TL} [L^3] is transmission losses estimated as the integral of the second term of Eq. (18). The total of Q_{TL} is restricted to the storage available in the aquifer:

$$Q_{TL} = \min[Q_{TL}, \max[(z - h) A S_y, 0]] \quad (20)$$

where: z is the surface elevation [L], h is water table elevation [L], A is the area of cell [L^2], and S_y is aquifer specific yield [-].

360 2.4 Unsaturated Component

Water infiltrated into the soil or through the stream channel becomes a flux input to the UZ (Fig. 1d). The unsaturated component comprises the soil and the riparian zone, both of which are simulated using a linear 'bucket' soil moisture balance model (Fig. 2a), following an approach similar to the FAO water balance model (Allen et al., 1998):

$$\Delta S_{UZ} = I + Q_{TL} - AET - R, \quad (21)$$

370 where: ΔS represents storage change [L], AET represents actual evapotranspiration rate [$L T^{-1}$] and R represents potential recharge rate [$L T^{-1}$]. The term Q_{TL} is only defined for stream cells. Diffuse potential recharge results from the local vertical percolation of the unsaturated zone, whereas focused potential recharge is produced in the riparian unsaturated zone (see Fig. 1).

375 Figure(2)

380 The amount of water available for plant evapotranspiration in the UZ, L [L], is estimated as the product of the rooting depth, D_{root} [L], and the volumetric water content, θ [$L^3 L^{-3}$]. The maximum amount of water that the soil can store is limited by the field capacity of the soil (L_{fc}), whereas the minimum amount is constrained by the wilting point (L_{wp}). Thus, the total available water, L_{TAW} , for plant transpiration is estimated by the difference between L_{fc} and L_{wp} (see Fig. 2).

385 The potential amount of water that plants can remove water from the UZ as transpiration, PET [$L T^{-1}$], which is the result of the product between a crop coefficient, k [-], and the reference potential evapotranspiration, ET_0 [$L T^{-1}$] (Allen et al., 1998). When there is enough water to supply plant energy demands, water can be extracted from the UZ at a rate equal to PET . However, when there is not enough water in the UZ to supply the PET , plants are considered to be under stressed conditions and the actual evapotranspiration (AET) is constrained as:

$$AET = I + \beta(PET - I) \quad (22)$$

390 where: β is a dimensionless parameter that depends on the water content and is estimated by:

$$\beta = \frac{L - L_{TAW}}{L_{TAW}(1 - c)} \quad (23)$$

395 where: c is the fraction of L_{TAW} [-] at which plants can extract water from the UZ without suffering water stress, and set to 0.5 as recommended by the FAO guidelines (Allen et al., 1998), although this can be varied in DRYP.

If, after accounting for infiltration and *AET*, there is a surplus of water in the soil that exceeds the field capacity, diffuse recharge (*R*) to the groundwater system occurs. If the model is run at daily time steps, we assume that all water content above field capacity will percolate and produce *R*. However, for sub-daily time steps, it is more realistic to assume that the soil slowly releases water as *R* when it is above the field capacity, depending on the soil water retention curve. Hence, in this case we assume that percolation to the water table depends on the water content and occurs only under the influence of gravity as follows:

$$D_{UZ} \frac{d\theta}{dt} = -K(\theta) \quad (24)$$

where $K(\theta)$ is estimated by using the Brooks and Corey (1964) relations and Clapp and Hornberger (1978) parameters (see Eq (3)):

$$K(\theta) = K_{sat} \left(\frac{\theta}{\theta_{sat}} \right)^{(2\lambda+2.5)} \quad (25)$$

We then substitute Eq. (25) into Eq. (24) and assume that the soil drains immediately into the groundwater component after evapotranspiration loss. Hence, an analytical solution based only on drainage without considering other inputs or outputs is specified by:

$$\theta = \exp \left(-(2\lambda - 1.5) \log \left| \theta^{-2\lambda-1.5} - \frac{\Delta t (2\lambda+1.5) K_{sat}}{D_{UZ} \theta_{sat}^{2\lambda+2.5}} \right| \right) \quad (26)$$

The UZ model component in DRYP can also change its behaviour when the head in the SZ component beneath restricts downward movement of water. This case is described below in Section 2.4 (Unsaturated – Saturated zone interactions).

The riparian zone uses, by default, the same hydraulic properties of the soil unsaturated zone except the saturated hydraulic conductivity which is assumed the same as the channel streambed K_{ch} , however, these parameters are also user-defined. The size of the riparian zone has a user-defined width (default is 20 m) and the length is the same as the stream.

2.5 Saturated Component

Lateral saturated flow underneath the unsaturated zone assumes the Dupuit-Forchheimer conditions for the Boussinesq equation and Darcian conditions for flow in/out of each model cell:

$$\frac{\partial h}{\partial t} + q_s + q_{riv} = \frac{1}{S_y} \nabla \cdot (-K_{sat} h \nabla h) + R - Q_{ASZ} \quad (27)$$

where: K_{aq} is the saturated hydraulic conductivity of the aquifer [$L T^{-1}$], S_y is the specific yield [-], q_s is saturation excess [$L T^{-1}$] (see Sect. 2.4.1), q_{riv} is discharge into stream [$L T^{-1}$] (see Sect. 2.4.2), Q_{ASZ} [$L T^{-1}$] is any groundwater abstraction, ∇ represents the gradient operator and $\nabla \cdot$ represents the divergence operator. Where the saturated thickness of the aquifer is relatively constant over the simulation period, transmissivity, T [$L^2 T^{-1}$], (the product of the aquifer thickness and the saturated hydraulic conductivity of the aquifer), may be held constant, hence linearising Eq. (25). Additionally, an exponential function based on Fan et al. (2013) has been added to represent the reduction of transmissivity in relation to depth:

$$T = K_{sat} f_D \exp \left(-\frac{z-h}{f_D} \right), \quad (28)$$

where: f_D is effective aquifer depth [L]. These different transmissivity parameterisation options can be toggled on or off in the main model control file.

445 Equation (27) is solved using a forward time central space (FTCS) finite difference approach. FTCS is an explicit finite difference approximation whose solution is sensitive to grid size and time step. Thus, in order to obtain a stable convergence of Eq. (27), a time variable approach was adopted. The maximum allowable time step for the saturated component is estimated based on the Courant number criteria (we use 0.25 as a default value but this may be changed by the user):

450

$$\frac{T\Delta t}{S_y \Delta x^2} \leq 0.25 \quad (29)$$

455 If the maximum time step of the SZ component is greater than the time step of the minimum time step of the any other component of the model, the time step of the SZ component is reduced to the time step of the minimum time step of the model (see Sect. 2.6 for more details of the model time step options).

2.5.1 Unsaturated - Saturated zone interactions

460 Unsaturated - saturated zone interactions are implemented using a variable depth unsaturated zone as follows (Fig. 3a). Unsaturated zone thickness (D_{uz}) is equal to the rooting depth when the water table elevation (h) is below the rooting depth, but when the water table is above the rooting depth the thickness of the unsaturated zone is reduced to the depth of the water table:

$$D_{uz} = \min[D_{root}, z - h] \quad (30)$$

465 When the water table is below the rooting elevation, z_{root} , there is no two-way interaction between the soil and the groundwater compartment (only one-way, as recharge), so no updates to the water table elevation are required (see Fig. 3a, left panel). However, when the water table crosses the z_{root} threshold, either via recharge or lateral groundwater flow, the water table is updated depending on the change in groundwater storage:

470

$$\frac{\Delta S_{SZ}}{\Delta t} = \nabla \cdot (-K_{sat} h \nabla h) + R - Q_{ASZ} \quad (31)$$

where: ΔS_{SZ} is the change in groundwater storage per unit area [$L^3 L^{-2}$]. Specifically, if an SZ cell is being recharged and the water table rises past the rooting depth in a given timestep, the water table is updated according to:

475

$$h_t = \frac{1}{\theta_{sat} - \theta_t} [\Delta S_{SZ} - (z_{uz} - h_{t-1}) S_y] + z_{uz} \quad (32)$$

whereas, when the water table is draining and passes the rooting depth in a given timestep:

$$h_t = -\frac{1}{S_y} [\Delta S_{SZ} - (h_{t-1} - z_{root})(\theta_{sat} - \theta_{fc})] + z_{root} \quad (33)$$

480

When the water table is above the rooting depth elevation, the water table elevation will be updated according to:

$$h_t = \frac{\Delta S_{SZ}}{\theta_{sat} - \theta_{fc}} + h_{t-1} \quad (34)$$

while if it is below the rooting depth elevation, the water table elevation is simply:

485

$$h_t = \frac{\Delta S_{SZ}}{S_y} + h_{t-1} \quad (35)$$

490 When the water table is above z_{root} , there is more water potentially available for evapotranspiration, since it can be taken from the groundwater reservoir via capillary rise or direct root water uptake. Thus, the potential maximum amount of water taken up from the groundwater reservoir, $PAET_{SZ}$ [$L T^{-1}$], is computed as the remaining PET after AET from the unsaturated component as:

$$PAET_{SZ} = PET - AET \quad (36)$$

495 For a shallow water table, upward capillary fluxes may also be taken from the groundwater reservoir. The rate of actual evapotranspiration from the SZ (AET_{SZ}), including both plant water uptake and capillary rise, is thus estimated as a linear function of the water table depth as follows:

$$AET_{SZ} = \max \left[PAET_{SZ} \left(\frac{h-z_{root}}{D_{root}} \right) \Delta t, 0 \right] \quad (37)$$

500

2.5.2 Surface–groundwater interactions

505 Surface - groundwater interactions are characterised in DRYP through transmission losses as described in Sect. 2.2.2. In addition, when the water table intersects a cell's defined streambed elevation it produces discharge into the stream, q_{riv} [L T⁻¹], and when the water table reaches the ground surface it produces saturation excess, q_s [L T⁻¹] (Fig. 3b) (Eq. (27)).

510 Discharge into streams, q_{riv} , is quantified using a head-dependent flux boundary condition (similar to that used in MODFLOW (Harbaugh, 2005)) as:

$$q_{riv} = C(h - h_{riv}) \quad (38)$$

where: C is a conductance term [L²T⁻¹] estimated as:

$$515 C = \frac{K_{ch}L_{ch}W}{0.25\Delta x} \quad (39)$$

To avoid numerical instabilities, we use a regularisation approach implemented via a smooth switch between the flux boundary condition and a constant head boundary (and vice versa) using a convex function (Marçais et al., 2017):

520

$$q_s = f_u \left(\frac{h-h_b}{z-h_b} \right) f_g (\nabla \cdot (-K_{sat}h \nabla h) + R - q_{riv}) \quad (40)$$

525

$$f_u = \exp \left(-\frac{1-u}{r} \right) \quad (41)$$

where r is a dimensionless regularisation factor $r > 0$, which has been specified as 0.001 following Marçais et al. (2017). f_g is the Heaviside step function.

530

$$f_g = \begin{cases} 0, & u < 0 \\ u, & u \geq 0 \end{cases} \quad (42)$$

535 After both q_s and q_{riv} are estimated, their corresponding volumes are estimated by multiplying the flow rate, the timestep and the corresponding surface area (cell or stream). The volume is then added as additional runoff in the surface component (Sect. 2.2.2). The water table is updated to its topographical elevation and kept as a constant head boundary condition. The boundary switches back to a flux condition if the water table drops back below the water table.

540

Figure(3)

2.6 Numerical implementation and time step

DRYP is a fully open-source, grid-based model with a layer-based structure, developed using the Landlab architecture (Hobley et al., 2017a) and its Python library. Landlab was chosen due to the versatility and its modular design that allows the user to plug in multiple modules for different levels of complexity and processes using grid-based objects (Barnhart et al., 2020; Hobley et al., 2017a).

Since most hydrological processes in DRYP, except the SZ component and the modified Green & Ampt infiltration, are described according to explicit-analytical solutions, it is possible to run DRYP at hourly or sub-hourly time steps at a low computational cost.

The three main DRYP components (i.e. surface, unsaturated and saturated components), can run at different time steps, from sub-hourly to daily. The riparian zone of the unsaturated component can be also run at a different time step to that of the unsaturated component. Where different time steps are used between components, the fluxes and state variables are temporally aggregated in DRYP by accumulating and/or averaging them over the specified time step as appropriate and then transferring them to the next component. In addition, and as described above, for the saturated component, an internal time step is also automatically considered to ensure the stability of the numerical solution.

560

3. Model Evaluation Methods

3.1 Evaluation using synthetic experiments

565 The use of synthetic experiments is an important aspect of model development in hydrology which is welcome but not used often (Clark et al., 2015). The objective of synthetic experiments is to better understand the structural controls on the physical processes represented in the model, for example, on groundwater-soil interactions (Batelis et al., 2020; Rahman et al., 2019). Here we perform a set of numerical experiments to evaluate the stability and convergence of DRYP components, particularly the coupling of both the surface and unsaturated zone with the groundwater component. Convergence and stability of the numerical solution of the groundwater component using 570 the FTCS finite difference approach and the regularization have been well documented in different studies (e.g. Anderson et al., (2015); Marçais et al., (2017); Wang and Anderson, (1982)). Hence, here we have considered two sets of model evaluations: (i) a quantitative evaluation of the model performance in relation to the well known numerical model, MODFLOW, for a simple surface-groundwater interaction test represented as a draining condition, and (ii) a qualitative evaluation of the model performance with respect to the desired skill of the model 575 to seamlessly allow interactions between groundwater and the land surface and surface water components.

(i) Comparing DRYP and MODFLOW

For the quantitative evaluation, a 1-D synthetic experiment considering an inclined plane aquifer was set-up using DRYP (see Fig 4a). The length and width of the model domain were specified as 10 km and 1 km, respectively. Hydraulic saturated conductivity and aquifer specific yield were specified as 1.2 m d^{-1} and 0.01, respectively. 580 Boundary conditions were specified as no-flow for both the right and left side as well as the bottom of the model domain. The model grid size was set to $1 \text{ km} \times 1 \text{ km}$.

A model with identical geometry, grid size and hydraulic properties was built in MODFLOW using the FLOPY python package (Bakker et al., 2016b, a). Boundary conditions for the MODFLOW model were the same as DRYP except for the top boundary condition, which was specified using the drain package (Harbaugh et al., 2000). The 585 elevation at which the water starts to drain was specified as the top surface elevation of the model domain. A high value of conductivity term ($500 \text{ m}^2 \text{ d}^{-1}$) was used in order to capture the seepage process and to assure convergence as well as minimal water balance errors (Batelaan and Smedt, 2004).

The synthetic test consisted of a free-draining condition for an unconfined aquifer with a water table depth equal 590 to zero (at the surface level). The time step used for evaluation was 1 day. The evaluation considered the temporal variation of the water table for both DRYP and MODFLOW models, as well as the water balance errors. Errors

were evaluated at all locations along the aquifer. Mass balance errors were estimated by the algebraic sum of inputs, outputs and the storage change.

(ii) Qualitative analysis of surface groundwater-interactions

The geometry of the model domain for the qualitative tests consisted of a tilted-V catchment (Fig. 4) with a size of 7×10 square cells on a 1-km resolution grid. Land use and soil hydraulic characteristics were specified as uniform over the entire model domain, and the saturated zone was considered as a homogenous and unconfined aquifer. Boundary conditions were specified as no-flow boundaries for all sides as well as at the bottom of the model domain. The initial water table was set as a horizontal plane at the level of the catchment outlet (100 m) for all simulations (Fig. 4). For experimental purposes, hydraulic characteristics of both the unsaturated and saturated zone were arbitrarily chosen. Thus, a loamy sand soil texture with $K_{sat} = 29.9 \text{ cm h}^{-1}$, $\theta_{sat} = 0.40$, $\theta_{fc} = 0.175$, and $\theta_{wp} = 0.075$ was chosen for the unsaturated zone, whereas, for the saturated zone, the hydraulic conductivity of the aquifer (K_{aq}) was specified as 6 m d^{-1} and the specific yield (S_y) was set as 0.01. The high value of K_{aq} combined with S_y and boundary conditions of the aquifer were applied in order to allow a fast increase/decrease of the water table and the observation of surface-groundwater interaction in a short period of time.

Three main scenarios were analysed by using synthetic time series of precipitation and evapotranspiration and changing hydraulic parameters of the UZ as follows:

1. An 'Infiltration - discharge' scenario, where all precipitation was allowed to infiltrate into the catchment and no infiltration excess was produced over the model domain.
2. An 'Infiltration-evapotranspiration-discharge' scenario was simulated by adding a time variable potential evapotranspiration as input into the model.
3. An 'Infiltration-runoff-evapotranspiration-discharge' scenario was designed to evaluate the production of runoff and focused groundwater recharge, as well as groundwater discharge. For this last scenario, the saturated hydraulic conductivity of the soil was decreased by one order of magnitude to produce infiltration excess and consequently, runoff.

For all three scenarios, precipitation events were specified at a constant value of $0.25 \text{ [mm h}^{-1}]$ over 10 days followed by a 20-day dry period. Potential evapotranspiration was specified as a sinusoidal function with a 24-hour period and a maximum rate of $0.10 \text{ [mm h}^{-1}]$. These experimental values of precipitation and evapotranspiration combined with the hydraulic properties of the unsaturated and saturated zone allowed a visual evaluation of surface-groundwater interactions under different conditions, such as increasing and decreasing water table through the model run and its interaction with the unsaturated zone.

Figure(4)

3.2 Model evaluation based on observed catchment data at Walnut Gulch, USA

In addition to evaluating the DRYP model with synthetic experiments, the model was also evaluated at the Walnut Gulch Experimental Watershed (WGEW), a 149 km^2 basin near Tombstone, Arizona, USA ($31^{\circ} 43'N$, $110^{\circ} 41'W$) (Fig. 5). The climate of the region is semi-arid with low annual rainfall, with a long-term average of 312 mm/yr (Goodrich et al., 2008). The ephemeral channels of WGEW are comprised of mixed sedimentary beds sourced that promote high transmission losses, leading to downstream declining discharge in all but the largest streamflow events (Michaelides et al., 2018; Singer and Michaelides, 2014). WGEW was chosen because it has a long and spatially explicit record of runoff (Stone et al., 2008) for multiple flumes as well as high density event-based rainfall data for 95 operational gauging stations (Goodrich et al., 2008) which were used to analyse trends in rainfall characteristics (Singer and Michaelides, 2017) and from which the STORM model was created (Singer et al., 2018). In addition, water content from a cosmic-ray neutron sensor as well as latent heat flux from Eddy covariance flux tower are also available in the basin (Emmerich and Verdugo, 2008; Zreda et al., 2012). Together these data provide an ideal opportunity to assess many components of a model of dryland water balance and partitioning (Emmerich and Verdugo, 2008; Goodrich et al., 2008; Keefer et al., 2008; Scott et al., 2015; Stone et

al., 2008). The water table at WGEW is deep (~50 m at the catchment outlet), so the potential interaction between surface and groundwater is generally unidirectional (Quichimbo et al., 2020).

Figure(5)

645

Model setting, inputs and parameters

650 For WGEW, model simulations were performed using the modified Green and Ampt infiltration approach because of its ability to describe the high potential infiltration rates at the beginning of the precipitation event, which is particularly important in this setting. The time step of both the surface component and unsaturated component was specified as one-hour, whereas we use a time step of one day for the riparian zone to reduce computational time. The high temporal resolution for the unsaturated component was used to capture the observed high intensity, low duration rainfall at WGEW, as well as the influence of diurnal fluctuations in evapotranspiration. Since the water table is deep below the ground surface and surface water groundwater interactions are known to be limited, the 655 groundwater component was not included in model simulations for WGEW.

660 Spatial and temporal information required as inputs and for model parameters were obtained for WGEW from <https://www.tucson.ars.ag.gov/dap/>. A model domain of 104×41 square cells on a 300-m resolution grid was developed. A digital elevation model with a spatial resolution of 30×30 metres was obtained from SRTM 1 Arc-Second Global map (available at <https://earthexplorer.usgs.gov>). The DEM was aggregated by averaging cells to the 300-m grid size. Textural characteristics of soil and land cover, obtained as polygon files from <https://www.tucson.ars.ag.gov/dap/>, were converted into model gridded inputs by considering the feature with the biggest area as the raster value. Based on the soil texture, baseline hydraulic properties required for modelling 665 were obtained from Rawls et al. (1982) and Clapp & Hornberger (1978). Values of field capacity and wilting point required to estimate L_{TAW} (Fig. 2a) were obtained assuming a matric potential of -33 kPa and -1500 kPa following the FAO guidelines (Walker, 1989).

670 Stream positions were estimated from the 30×30 m DEM. The routing network at the 30×30 m grid resolution was specified by defining a minimal upstream drainage area threshold of 65ha, which corresponds to the medium 675 stream network resolution specified in Heilman et al. (2008). Stream cells were then aggregated to the model grid size, 300×300 m, to obtain the stream length at any given cell. Stream width was assumed as 10 m for the whole model domain based on average values observed across the whole catchment (Miller et al., 2000). Point measurements of rainfall were obtained from 95 rainfall stations well distributed within the basin (Goodrich et al., 2008). Rainfall data, at every location, were temporally aggregated to 1-hour and then spatially interpolated using 680 a Natural Neighbour algorithm to a 30×30 m grid size to preserve the high spatial and temporal variability of station located at distances smaller than the model grid size. Finally, rainfall was spatially aggregated to the grid size of the model domain. Potential evapotranspiration (PET) was calculated using hourly data from ERA5-Land reanalysis (Hersbach et al., 2020) because this dataset enabled high temporal resolution (1-hour) and its potential to drive hydrological and land surface models (Albergel et al., 2018; Alfieri et al., 2020; Tarek et al., 2020; Singer et al., 2021). Data from ERA5 have a spatial resolution of ~9 km at the equator. The Penman-Monteith approach was chosen to estimate hourly PET due to its high accuracy to produce evapotranspiration values under different climates and locations, and also because it is considered a standard method by the FAO (Food and Agriculture Organization of the United Nations) (Allen et al., 1998).

685 High-resolution temporal measurements of runoff at three flumes (F01, F02, and F06) along the main Walnut Gulch channel were used in the evaluation of runoff generation (Fig. 5). To evaluate modelled soil moisture, we used data from a cosmic-ray neutron sensor station from the COSMOS network (Zreda et al., 2012), located within the Kendall subcatchment of WGEW (Fig. 5). The raw data (publicly available at <http://cosmos.hwr.arizona.edu/Probes/StationDat/010/index.php>) were corrected for atmospheric pressure (Hidroinnova, 2013), atmospheric vapour pressure (Rosolem et al., 2013), above ground biomass and variation in background intensity using the standardized data processing Cosmic-Ray Sensor PYthon tool (Power et al., 2021) for the period between mid-2010 and 2018.

Finally, data from the Ameriflux site Kendall Grassland (US-Wkg; available at <https://ameriflux.lbl.gov/sites/siteinfo/US-Wkg>), were used for evaluation of simulated *AET* (Fig. 5). Uncertainty in flux tower data is mainly attributed to instrumental and random errors and it increases with flux magnitude (Richardson et al., 2006; Schmidt et al., 2012). Mean relative errors for AmeriFlux sites are around -5 % with deviations of ± 16 % (Schmidt et al., 2012). Historical records from mid-2006 to 2018 were available for model evaluation.

700 **Model sensitivity analysis and calibration**

An initial trial-and-error calibration of the model was performed to explore the parameter sensitivities of DRYP and to reduce the a-priori parameter ranges used in the second step. This first trial-and-error calibration considered only the performance of the model to represent streamflow at the catchment outlet (flume F01). The calibration was performed by applying spatially constant multiplicative factors kW , KK_{sat} , kD , KK_{ch} , kk_T , to model parameters W , K_{sat} , D , K_{ch} and k_T , respectively. These parameters were used because they control the storage and the water partitioning of components (surface and subsurface components) in the DRYP model for WGEW. Parameters W , K_{ch} and k_T were assumed to be uniform over the entire catchment due to the lack of spatial information, whereas the rest of parameters listed in Table 1 vary depending on their mapped spatial distribution. The initial manual calibration enabled a set of parameter ranges to be defined for a Monte Carlo experiment to analyse the multi-parameter uncertainty of the model results. Then, a set of 1000 realisations was implemented for the analysis with parameters randomly generated using a uniform distribution.

The Generalized Likelihood Uncertainty Estimation (GLUE) framework (Beven and Binley, 1992) was used as the uncertainty analysis framework. The GLUE framework considers that, owing to the uncertainty of the input data, model structure and limitations of boundary condition, there are multiple set of parameters that can produce acceptable simulations. To determine which simulations were considered as acceptable (i.e. behavioural), we used a combination of two different 'goodness of fit' indices: Nash–Sutcliffe Efficiency (NSE) (Nash and Sutcliffe, 1970), and per cent bias (PBIAS) defined as follows:

$$720 \quad NSE = 1 - \frac{\sum_{i=1}^n (O_i - S_i)^2}{\sum_{i=1}^n (O_i - \bar{O})^2} \quad (43)$$

$$PBIAS(\%) = 100 \cdot \frac{\sum_{i=1}^n O_i - \sum_{i=1}^n S_i}{\sum_{i=1}^n O_i} \quad (44)$$

725 where: O represents the observation, \bar{O} is the arithmetic mean of observations, S represents the model simulations, and n is the number of observations.

In order to define behavioural models, a set of thresholds was specified for the three indices. For streamflow, values of NSE higher than 0.50 and PBIAS less than 20 % (i.e. less than 1 % of the total water budget of the study 730 area) were considered as acceptable simulations. For soil moisture and actual evapotranspiration, only values of NSE greater than 0.5 were also set.

In order to combine these measures into a single performance metric, models which did not meet these conditions 735 were assigned a value of zero, whereas the indexes were linearly scaled between 0 and 1 for rest of models. Scaling of NSE values was performed according to the following range: 0 for the minimum value ($NSE = 0.5$) and 1 for the maximum value of NSE which is also 1. For PBIAS, absolute values were scaled by considering the maximum value ($PBIAS = 20$ %) equal to 0 and the minimum ($PBIAS = 0$) equal to 1. The combined performance measure was calculated as the product of all indexes considered in the analysis:

$$740 \quad p_i = \prod_{k=1,2,6} NSE_k^* \cdot PBIAS_k^* \quad (45)$$

where p^* is the combined performance measure for the i -th parameter set, the $*$ signifies scaled values, and k represents the variable considered in the analysis.

745 For soil moisture, a direct comparison between observation and simulations was not possible due to differences between the representative soil depths of measurements and simulations. Modelled soil moisture represents the water content of the entire soil column specified by the rooting depth, whereas the observed soil moisture represents the water content over a depth-averaged value, which can be characterized by an effective soil depth that depends on the soil moisture itself (Franz et al., 2012). A direct comparison would result in the
750 misrepresentation of high values of observed soil water content by the model due to the attenuation of peak values over larger soil depths. This problem has been solved by using exponential models that need to be calibrated by using measurements at different soil depths (e.g. Albergel et al., (2008); Wagner et al. (1999)). Therefore, to enable model-data comparisons that capture the variation of both high and low values of soil moisture observations, we scaled observed soil moisture by the following expression:

755

$$O^* = O^\alpha + S_{min} \quad (46)$$

where: * refers to the scaled value, and α is estimated by:

760

$$\alpha = \frac{\log|S_{max} - S_{min}|}{\log|O_{max} - O_{min}|} \quad (47)$$

The period between 01/01/2007 and 01/01/2018 was the temporal domain for model simulations at WGEW, with a warm-up period of one year prior to this period. This period matches the overlapping period of streamflow observations and flux tower observations. Soil moisture was evaluated for a shorter period of available data
765 01/10/2010 and 01/01/2018. Additionally, modelled soil moisture for COSMOS site was obtained by spatial averaging the 9 cells located around the COSMOS station to match the effective COSMOS footprint diameter (~700m) (Desilets and Zreda, 2013).

4. Results

770

4.1.1. Comparing DRYP to MODFLOW

The modelling results show a good agreement between DRYP and MODFLOW and both models ran with negligible mass balance errors (1.79e-15 m³ for DRYP, and 6.95e-8 m³ for MODFLOW) (see Fig. 6). Both the temporal and spatial variations in the MODFLOW model are well captured by DRYP. Differences in water table elevations are in the range of just 0.022 m at the beginning of the simulation when the aquifer starts to drain, and these differences only decrease as the water table decreases (see Fig. 6a). Temporal variation of the groundwater storage for both models show consistency, with higher values due to high gradients at the beginning of the simulation, decreasing as the water table decreases (see Fig. 6b). More fluctuations are observed in the MODFLOW simulations, which can be attributed to the time step used for the simulation, which needs to be reduced in order to smoothly capture the variation in water table depth as the model switches boundary conditions. DRYP captures this variation smoothly due to the exponential function and by automatically reducing the time step to assure numerical convergence.

785 Figure (6)

4.1.2. Evaluation of qualitative synthetic experiments

790 Figure 7 shows the temporal variation of fluxes and state variables for the three simulated scenarios at two evaluation points located along the channel, one at the catchment outlet and the second 4 km from the catchment outlet. These results are in turn described below:

1. 'Infiltration - discharge' scenario (blue lines): when the precipitation falls over the catchment (Fig. 6a) it immediately infiltrates into the unsaturated zone, increasing the water content of the soil. Since there are no losses due to evapotranspiration, the water content steadily increases until it reaches field capacity (Fig. 7b). At field capacity, given that the soil cannot hold any excess water, it starts to release water as diffuse recharge. The soil remains at field capacity for the rest of the simulation, allowing the water from the next rainfall event to move directly to the saturated zone producing recharge (Fig. 7c). Recharge produces an increase in groundwater storage and consequently increases the discharge at the outlet of the catchment (Fig. 7d). In the early precipitation events, the contribution of groundwater discharge is minimal. However, this contribution keeps increasing until a dynamic steady-state is eventually reached (by 14600 hours, not shown in Fig. 7). Discharge closely follows the temporal variation of the precipitation, due to the high transmissivity of the aquifer and the saturation of the soil; a sharp increase in discharge means that precipitation has become the main contributor to discharge changes because the water table is at the surface (Fig. 7d).
2. 'Infiltration-evapotranspiration-discharge' (green lines): the addition of evapotranspiration in this experiment produces a reduction in soil water content (Fig. 7b). Since precipitation is much higher than evapotranspiration, soil moisture quickly reaches a dynamic steady-state at the end of the second precipitation event. At cells located close to the catchment outlet, the rise of the water table to ground level reduces the thickness of the unsaturated zone to zero, as no water can be infiltrated, the soil water content is kept at its highest value during the precipitation event. After the precipitation event, the rate of evapotranspiration, which is greater than the rate of lateral groundwater inflow, gradually reduces the amount of water in the cell. However, since the storage of the SZ keeps increasing, the thickness of the UZ decreases and the rate of lateral groundwater flow becomes greater than the rate of evapotranspiration, it also results in quick changes in the water content of the soil (Fig. 7b). Recharge is also reduced and, as expected, it only occurs when the soil moisture reaches field capacity (Fig. 7c). Discharge is also reduced as a result of decreased aquifer recharge due to upward losses by AET. For cells close to saturation, the storage in the groundwater reservoir is affected by evapotranspiration losses (not observed in right panel due to the y-axis scale), which in turn results in daily fluctuations in discharge that are inverse of evapotranspiration fluctuations.

3. 'Infiltration-runoff-evapotranspiration-discharge' scenario (red lines): a reduced K_{sat} results in the development of infiltration excess overland flow. The rate of infiltration at the beginning of the precipitation event is high enough to provide water for evapotranspiration without reducing the soil water storage (Fig. 7b), which explains the similarity in soil moisture behaviour with the second scenario. When cells start to produce runoff as a result of infiltration-excess, discharge also starts to rise. At stream cells with a deep water table, the increase in streamflow is the result of flow accumulation along the channel during the precipitation event (e.g. Fig. 7d, left panel at 6600 to 6700 hours). At cells where the water table interacts with the surface, groundwater discharge increases gradually the streamflow at the catchment outlet at much longer temporal scales (Fig. 7d). At the catchment outlet, streamflow is also affected by the fluctuation of the water table due to the daily variation of evapotranspiration losses (Fig. 7d).

Figure (7)

Figure 8 shows the cumulative volumes of different components of the water balance as well as the cumulative mass balance error of the model. Mass balance errors are low in comparison to the total amount of water entering the catchment, with values less than 0.12 % for the first case (only precipitation). For the other two cases where evapotranspiration is included, errors are less than 0.02 %. The higher error for the first case scenario is attributed to the concentration of flow at the catchment outlet, which leads to an increase in the number of cells discharging into the surface and the channel and the resulting minor numerical artifacts.

Figure (8)

Coupling of surface and groundwater processes often results in numerical instabilities and in convergence problems (Batelaan and Smedt, 2004; Marçais et al., 2017). However, the results of these synthetic experiments illustrate DRYP's ability to produce realistic hydrological process behaviours by providing a stable solution for representing surface-groundwater interactions without producing numerical artifacts. DRYP is effective at handling the complex coupling and dynamic switching of different types of hydraulic boundary conditions, producing acceptable results with negligible mass balance errors.

4.2. Model performance at WGEW

4.2.1. Spatio-temporal visualisation of model process simulation at WGEW

The ability of the model to capture the dynamics of dryland hydrological processes is illustrated for WGEW in Figure 9. The best model (see following section) captures the emergence of ephemeral flow conditions for specific storms, as well as the spatio-temporal changes in soil moisture. It can be seen how, for a given initial soil moisture condition, the production of runoff due to a rainfall event falling over only the central part of catchment results in the concentration of flow along the stream. As water moves downstream, the stream loses water due to transmission losses, which ultimately consumes almost all the available water by the time runoff reaches the catchment outlet (flume F01 in Figure 9c).

Figure(9)

4.2.1. Characterisation of the temporal variation in simulated variables

Calibration using the trial-and-error method, showed that streamflow showed particular sensitivity to the parameters K_{sat} , D , K_{ch} and k_T . This informed a set of parameters ranges that were used in the Monte Carlo analysis as follows: for hydraulic conductivity at the channel, kK_{ch} 0.10 and 0.30, for kK_{sat} 0.20 and 0.50, for kk_T 3-10, and kD 0.80 and 1.20. This resulted in 21 behavioural models with values of p above zero. The calibrated parameters for the best simulation were $kK_{ch} = 0.21$, $kAWC = 1.02$, $kK_{sat} = 0.30$, and $kk_T = 7.7$. A factor of $kk_T = 7.7$ applied to default value of k_T (0.083) represents a flow velocity of 0.41 m s^{-1} in the channel.

Soil moisture

875 The DRYP model demonstrates skill at capturing the dynamics of the soil moisture (Fig. 10b) with values of NSE around 0.69. Discrepancies in the magnitude of peak values are likely the result of scaling, so simulations are not able to account for the variation of the effective measurement depth of COSMOS water content estimates (Franz et al., 2013, 2012). The effective COSMOS measurement depth is greater for low values of soil water content (around 33 cm), whereas, for higher values of water content the effective measurement depth is shallow (around 880 16 cm). However, discrepancies may also reflect the limited ability of the soil moisture model to represent high variations occurring at shallow depths of the soil layer, due to the use of a single store.

Evapotranspiration

885 The DRYP model also captures well (NSE ~0.7) the seasonality and the overall temporal variation in evapotranspiration, a dominant component of the water budget in drylands (Fig. 10c), although peak values are generally overpredicted after long periods of dry conditions. Nevertheless, discrepancies between flux tower data and simulated *AET* up to 15% for one year have been reported for grassland vegetation in previous studies (Scott, 2010; Twine et al., 2000), and such errors are mainly attributed to the inherent uncertainty in rainfall and latent heat flux measurements (Scott, 2010).

890

Streamflow

DRYP is also able to reproduce the seasonality and the monthly production of runoff at the outlet of the catchment (F01, NSE ~0.9) (Fig. 10f), as well as at the two upstream flumes (F02, F06) considered in the analysis (NSE > 0.60) (Figs. 10d and 10e). However, monthly values at flumes F02 and F06 are overpredicted in 2012, perhaps reflecting the development of a crusting layer in previous dry years (e.g. 2009, 2011), a process not included in the model. On the other hand, low production of runoff during wet years (e.g. 2015) may be attributed to the energy of high intensity rainfall events removing such a crusting layer from the top of the soil, which in turn results in the increase of infiltration rates (Becker et al., 2018). Additionally, the spatial aggregation of the DEM causes slight inaccuracies in the estimated contributing areas for different streams. This affects not only the volume but 900 also the timing of streamflow events, which may result in over/under prediction of streamflow events and may ultimately affect the overall water budget.

Figure (10)

905 Water balance

Precipitation shows high annual variability for the evaluated period, with the lowest value of 200 mm y^{-1} in 2011 up to 400 mm y^{-1} in 2015 (Fig. 10a), which translates into variability in the annual water partitioning for WGEW. For the evaluation period, 01/01/2007 to 01/01/2018, water balance estimates from the best model show that ~92 % of the total precipitation infiltrates into the soil (see Fig. 11). However, almost all infiltrated water returns to the atmosphere as evapotranspiration losses, representing 89 % of the total precipitation. A small proportion, ~3 % of the total precipitation, remains in the soil, and this stored water corresponds mainly to wetter years of the simulation period (2014, and 2015). Only a small percentage, less than 0.03 %, percolates as diffuse recharge contributing to groundwater storage. Water that does not infiltrate into the soil (8 % of the precipitation) is routed downstream. However, this amount of water is consistently reduced by transmission losses, representing ~7 % of the precipitation. Water entering the riparian zone via transmission losses is partitioned into evapotranspiration and focused recharge. Evapotranspiration consumes up to 60 % of these transmission losses representing ~4.5 % of the total precipitation. This is broadly consistent with previous studies showing values of 20 mm y^{-1} or 5.5 to 7 % of the total precipitation (Renard, 1970; Renard et al., 2008). The amount of surface water leaving the catchment represents less than 1.0 % of the total amount of precipitation falling over the catchment. These values highlight 915 920 the impact of transmission losses on the streamflow and aquifer recharge. The main contributor to the total amount of groundwater recharge is focused recharge (~2.5 % of precipitation).

Figure(11)

925 **5. Conclusions**

We have developed and presented a parsimonious model to estimate water partitioning in dryland regions (“DRYP”). We have provided a technical description of all components of DRYP and evaluated it under different scenarios. We first evaluated the ability of DRYP to provide stable numerical simulations of the interaction of 930 surface and subsurface components through synthetic model experiments. Then, we evaluated DRYP using streamflow, soil moisture, and evapotranspiration data from the semi-arid Walnut Gulch Experimental Watershed (Arizona, USA). We tested the ability of the model to produce behavioural simulations based on multi-parameter Monte-Carlo experiments evaluated against a range of objective performance metrics. A comparison between DRYP and MODFLOW for a simple draining-case model showed an excellent agreement with an error in 935 hydraulic head of < 0.022 m, and mass balance error of 6.95e-8 m³. An evaluation of surface-groundwater interactions using numerical experiments over a synthetic model domain indicated that DRYP shows skill at producing stable simulations for the main components of the water balance with low mass balance errors (< 0.12 %). Thus, we conclude that DRYP has the potential to be robustly applied in environments where surface-subsurface interactions play an important role in the overall mass balance of the catchment.

940 For Walnut Gulch, DRYP effectively captures the spatio-temporal variability of the main components of the dryland water balance at monthly time scales. We find that focused recharge represents ~2.5 % of the total amount of rainfall, whereas diffuse recharge is below 0.03 %. Evapotranspiration is the dominant process representing 945 90% of water leaving the catchment. Evapotranspiration from riparian areas also plays an important role in groundwater recharge since the amount of water becoming focussed recharge is only around ~40% of the transmission losses.

950 Finally, considering the combination of explicit solutions of surface and subsurface components, the parsimonious structure, and the low computational cost, it is possible for DRYP to perform long runs using hourly or sub-hourly time steps. These characteristics enable DRYP to test long-term and seasonal changes in water availability to 955 plants and humans in limited water environments under different scenarios and future climatic conditions such as anthropogenic activities or during droughts.

960 Furthermore, improving the soil-vegetation interaction in the unsaturated zone to capture the temporal variation of plant water demand will likely enhance the performance of the model. A more complex representation of the highly dynamic behaviour of ephemeral streamflow will be considered in future developments in order to enhance the ability of the model to represent flooding conditions. Additionally, we also plan to use DRYP in conjunction with stochastic rainfall simulation tools (such as STORM, Singer et al. (2018)) to explore the impact of the variability of precipitation on the water balance.

965 **Acknowledgements**

EAQ gratefully acknowledges financial support from Cardiff University through a Vice Chancellor’s Scholarship. MOC gratefully acknowledges funding for an Independent Research Fellowship from the UK Natural Environment Research Council (NE/P017819/1). MBS acknowledges funding from the U.S. National Science Foundation (BCS-1660490, EAR-1700517) and the U.S. Department of Defense’s Strategic Environmental Research and Development Program (RC18-1006). The team also acknowledge funding from the Global Challenges Research Fund (GCRF) (‘Impacts of Climate Change on the Water Balance in East African Drylands’); The Royal Society (‘DRIER’, CHL\R1\180485); and the European Union’s Horizon 2020 Programme (‘DOWN2EARTH’, 869550).

970

Code availability.

DRYP is available for download at <https://doi.org/10.5281/zenodo.5061987> (last access: 26 Mar 2021)

Data availability.

975 Our dataset contains modified Copernicus Climate Change Service information [1981-present. The model data used in this research is publicly available from <https://www.tucson.ars.ag.gov/dap/>.

Author contributions.

EAQ, implementation, conceptualization and data analysis, MOC conceptualization and data analysis. MBS conceptualization and data analysis. KM conceptualization and data analysis. DH conceptualization, implementation, and data analysis. RR conceptualization and data analysis. The paper was written by EAQ with contributions from all co-authors.

980 Competing interests.

The authors declare that they have no conflict of interest.

985 Disclaimer.

Any use of trade, firm, or product names is for descriptive purposes only and does not imply endorsement by the Cardiff University.

List of parameters and model variables

Parameter	Description	Dimension
AET	Actual evapotranspiration	[L T ⁻¹]
AET_{sz}	Capillary rise	[L T ⁻¹]
B	Initial suction head	[L]
C	River conductivity	[L ² T ⁻¹]
c	Readily available water factor	[·]
D_{root}	Rooting depth	[L]
D_{uz}	Unsaturated zone thickness	[L]
ET_0	Reference evapotranspiration	[L T ⁻¹]
f	Infiltration rate	[L T ⁻¹]
fd	Effective aquifer depth (for exponential function)	[L]
h	Water table elevation	[L]
h_b	Aquifer bottom elevation	[L]
h_{riv}	River stage elevation	[L]
I	Cumulative infiltration	[L]
I_c	Cumulative infiltration capacity	[L]
ich	Channel losses	[L ³ T ⁻¹]
k	Crop coefficient	[·]
K_{aq}	Aquifer Saturated hydraulic conductivity	[L T ⁻¹]
K_{ch}	Channel saturated hydraulic conductivity	[L T ⁻¹]
kdt	Schaake reference parameter	[·]
K_{dtref}	Reference hydraulic conductivity	[L T ⁻¹]
K_{sat}	Saturated hydraulic conductivity	[L T ⁻¹]
k_T	Recession time for channel streamflow	[T ⁻¹]
L	Water thickness in the unsaturated zone	[L]
L_{ch}	Channel length	[L]
P	Precipitation	[L]
p	Precipitation rate	[L T ⁻¹]
$PAET_{sz}$	Maximum water uptake from saturated zone	[L T ⁻¹]
PET	Potential evapotranspiration	[L T ⁻¹]
q_0	Initial volumetric flow rate	[L ³ T ⁻¹]
Q_{ASW}	Surface water abstraction	[L ³]
Q_{ASZ}	Groundwater abstraction	[L T ⁻¹]
Q_{in}	Channel inflow	[L ³]
q_{in}	Volumetric flow rate entering stream cell	[L ³ T ⁻¹]
Q_{out}	Channel outflow	[L ³]

q_{rir}	Saturation excess overland flow	[L T ⁻¹]
q_s	Groundwater discharge into streams	[L T ⁻¹]
Q_{TL}	Transmission losses	[L ³]
R	Groundwater recharge	[L T ⁻¹]
r	Regularisation factor	[\cdot]
S_p	Sorptivity	[L ² T ^{1/2}]
S_{sw}	Channel storage	[L ³]
S_{sz}	Storage in the saturated zone	[L]
S_{uz}	Storage in the unsaturated zone	[L]
S_y	Specific yield	[\cdot]
T	Aquifer Transmissivity	[L ² T ⁻¹]
TAW	Total available water for plant evapotranspiration	[L]
W	Channel width	[L]
z	Surface elevation	[L]
z_{riv}	Bottom channel elevation	[L]
β	Water stress coefficient	[\cdot]
θ_{fc}	Water content at field capacity	[\cdot]
θ_{sat}	Saturated water content	[\cdot]
θ_{wp}	Water content at wilting point	[\cdot]
λ	Soil pore size distribution	[\cdot]
μ_y	Log mean saturated hydraulic conductivity	[L T ⁻¹]
σ_y	Standard deviation of the log saturated hydraulic	[L T ⁻¹]
ψ_a	Initial suction head	[L]
ψ_f	Suction head	[L]

990 References

Abbott, M. B., Bathurst, J. C., Cunge, J. A., O'Connell, P. E., and Rasmussen, J.: An introduction to the European Hydrological System — Systeme Hydrologique European, "SHE", 2: Structure of a physically-based, distributed modelling system, *J. Hydrol.*, 87, 61–77, [https://doi.org/10.1016/0022-1694\(86\)90115-0](https://doi.org/10.1016/0022-1694(86)90115-0), 1986.

995 Abdulrazzak, M. J.: Losses of flood water from alluvial channels, *Arid Soil Res. Rehabil.*, 9, 15–24, <https://doi.org/10.1080/15324989509385870>, 1995.

Albergel, C., Rüdiger, C., Pellarin, T., Calvet, J.-C., Fritz, N., Froissard, F., Suquia, D., Petitpa, A., Piguet, B., and Martin, E.: From near-surface to root-zone soil moisture using an exponential filter: an assessment of the method based on in-situ observations and model simulations, *Hydrol. Earth Syst. Sci.*, 12, 1323–1337, <https://doi.org/10.5194/hess-12-1323-2008>, 2008.

1000 Albergel, C., Dutra, E., Munier, S., Calvet, J.-C., Munoz-Sabater, J., de Rosnay, P., and Balsamo, G.: ERA-5 and ERA-Interim driven ISBA land surface model simulations: which one performs better?, *Hydrol. Earth Syst. Sci.*, 22, 3515–3532, <https://doi.org/10.5194/hess-22-3515-2018>, 2018.

1005 Alfieri, L., Lorini, V., Hirpa, F. A., Harrigan, S., Zsoter, E., Prudhomme, C., and Salamon, P.: A global streamflow reanalysis for 1980–2018, *J. Hydrol. X*, 6, 100049, <https://doi.org/10.1016/j.hydroa.2019.100049>, 2020.

Allen, R. G., Pereira, L. S., Raes, D., and Smith, M.: Crop evapotranspiration-Guidelines for computing crop water requirements-FAO Irrigation and drainage paper 56, FAO Rome, 300, D05109, 1998.

1010 Anderson, M. P., Woessner, W. W., and Hunt, R. J.: *Applied Groundwater Modeling: Simulation of Flow and Advection Transport*, Academic Press, 632 pp., 2015.

1015 Aryal, S. K., Silberstein, R. P., Fu, G., Hodgson, G., Charles, S. P., and McFarlane, D.: Understanding spatio-temporal rainfall-runoff changes in a semi-arid region, *Hydrol. Process.*, 34, 2510–2530, <https://doi.org/10.1002/hyp.13744>, 2020.

1015 Assouline, S.: Infiltration into soils: Conceptual approaches and solutions, *Water Resour. Res.*, 49, 1755–1772, <https://doi.org/10.1002/wrcr.20155>, 2013.

1020 Bakker, M., Post, V., Langevin, C. D., Hughes, J. D., White, J., Starn, J., and Fienen, M. N.: FloPy: Python package for creating, running, and post-processing MODFLOW-based models, U.S. Geological Survey, <https://doi.org/10.5066/F7BK19FH>, 2016a.

1020 Bakker, M., Post, V., Langevin, C. D., Hughes, J. D., White, J. T., Starn, J. J., and Fienen, M. N.: Scripting MODFLOW Model Development Using Python and FloPy, *Groundwater*, 54, 733–739, <https://doi.org/10.1111/gwat.12413>, 2016b.

1025 Barnhart, K. R., Hutton, E. W. H., Tucker, G. E., Gasparini, N. M., Istanbulluoglu, E., Hobley, D. E. J., Lyons, N. J., Mouchene, M., Nudurupati, S. S., Adams, J. M., and Bandaragoda, C.: Short communication: Landlab v2.0: a software package for Earth surface dynamics, *Earth Surf. Dyn.*, 8, 379–397, <https://doi.org/10.5194/esurf-8-379-2020>, 2020.

1025 Batelaan, O. and Smedt, F. D.: SEEPAGE, a New MODFLOW DRAIN Package, *Groundwater*, 42, 576–588, <https://doi.org/10.1111/j.1745-6584.2004.tb02626.x>, 2004.

1030 Batelis, S.-C., Rahman, M., Kollet, S., Woods, R., and Rosolem, R.: Towards the representation of groundwater in the Joint UK Land Environment Simulator, *Hydrol. Process.*, 34, 2843–2863, <https://doi.org/10.1002/hyp.13767>, 2020.

1030 Becker, R., Gebremichael, M., and Märker, M.: Impact of soil surface and subsurface properties on soil saturated hydraulic conductivity in the semi-arid Walnut Gulch Experimental Watershed, Arizona, USA, *Geoderma*, 322, 112–120, <https://doi.org/10.1016/j.geoderma.2018.02.023>, 2018.

1035 Beven, K. and Binley, A.: The future of distributed models: model calibration and uncertainty prediction, *Hydrol. Process.*, 6, 279–298, 1992.

1035 Braun, J. and Willett, S. D.: A very efficient O(n), implicit and parallel method to solve the stream power equation governing fluvial incision and landscape evolution, *Geomorphology*, 180–181, 170–179, <https://doi.org/10.1016/j.geomorph.2012.10.008>, 2013.

1040 Brooks, R. H. and Corey, A. T.: *Hydraulic Properties of Porous Media*, Colorado State University, 40 pp., 1964.

1040 Chen, F. and Dudhia, J.: Coupling an Advanced Land Surface–Hydrology Model with the Penn State–NCAR MM5 Modeling System. Part I: Model Implementation and Sensitivity, *Mon. Weather Rev.*, 129, 569–585, [https://doi.org/10.1175/1520-0493\(2001\)129<0569:CAALSH>2.0.CO;2](https://doi.org/10.1175/1520-0493(2001)129<0569:CAALSH>2.0.CO;2), 2001.

1045 Cherlet, M., Hutchinson, C., Reynolds, J., Hill, J., Sommer, S., and von Maltitz, G.: *World atlas of desertification*. Luxembourg: Publication Office of the European Union, 3rd ed., Luxembourg, 295 pp., 2018.

1045 Chow, V. T., Maidment, D. R., and Mays, L. W.: *Applied Hydrology*, Mc Graw Hill, 588 pp., 1988.

1050 Clapp, R. B. and Hornberger, G. M.: Empirical equations for some soil hydraulic properties, *Water Resour. Res.*, 14, 601–604, <https://doi.org/10.1029/WR014i004p00601>, 1978.

1050 Clark, M. P., Fan, Y., Lawrence, D. M., Adam, J. C., Bolster, D., Gochis, D. J., Hooper, R. P., Kumar, M., Leung, L. R., Mackay, D. S., Maxwell, R. M., Shen, C., Swenson, S. C., and Zeng, X.: Improving the

representation of hydrologic processes in Earth System Models, *Water Resour. Res.*, 51, 5929–5956, <https://doi.org/10.1002/2015WR017096>, 2015.

1055 Coes, A. L. and Pool, D. R.: Ephemeral-stream channel and basin-floor infiltration and recharge in the Sierra Vista subwatershed of the Upper San Pedro Basin, Southeastern Arizona: Chapter J in Groundwater recharge in the arid and semiarid southwestern United States (Professional Paper 1703), U.S. Geological Survey, 2007.

Craig, J. R., Liu, G., and Soulis, E. D.: Runoff–infiltration partitioning using an upscaled Green–Ampt solution, *Hydrol. Process.*, 24, 2328–2334, <https://doi.org/10.1002/hyp.7601>, 2010.

1060 Cuthbert, M. O., Acworth, R. I., Andersen, M. S., Larsen, J. R., McCallum, A. M., Rau, G. C., and Tellam, J. H.: Understanding and quantifying focused, indirect groundwater recharge from ephemeral streams using water table fluctuations, *Water Resour. Res.*, 52, 827–840, <https://doi.org/10.1002/2015WR017503>, 2016.

1065 Cuthbert, M. O., Gleeson, T., Moosdorf, N., Befus, K. M., Schneider, A., Hartmann, J., and Lehner, B.: Global patterns and dynamics of climate–groundwater interactions, *Nat. Clim. Change*, 9, 137–141, <https://doi.org/10.1038/s41558-018-0386-4>, 2019a.

1070 Cuthbert, M. O., Taylor, R. G., Favreau, G., Todd, M. C., Shamsudduha, M., Villholth, K. G., MacDonald, A. M., Scanlon, B. R., Kotchoni, D. O. V., Vouillamoz, J.-M., Lawson, F. M. A., Adjomayi, P. A., Kashaigili, J., Seddon, D., Sorensen, J. P. R., Ebrahim, G. Y., Owor, M., Nyenje, P. M., Nazoumou, Y., Goni, I., Ousmane, B. I., Sibanda, T., Ascott, M. J., Macdonald, D. M. J., Agyekum, W., Koussoubé, Y., Wanke, H., Kim, H., Wada, Y., Lo, M.-H., Oki, T., and Kukuric, N.: Observed controls on resilience of groundwater to climate variability in sub-Saharan Africa, *Nature*, 572, 230–234, <https://doi.org/10.1038/s41586-019-1441-7>, 2019b.

1075 Datry, T., Bonada, N., and Boulton, A. (Eds.): *Intermittent Rivers and Ephemeral Streams, Ecology and Management*, Academic Press, <https://doi.org/10.1016/B978-0-12-803835-2.09997-6>, 2017.

Desilets, D. and Zreda, M.: Footprint diameter for a cosmic-ray soil moisture probe: Theory and Monte Carlo simulations, *Water Resour. Res.*, 49, 3566–3575, <https://doi.org/10.1002/wrcr.20187>, 2013.

1080 Emmerich, W. E. and Verdugo, C. L.: Long-term carbon dioxide and water flux database, Walnut Gulch Experimental Watershed, Arizona, United States, *Water Resour. Res.*, 44, <https://doi.org/10.1029/2006WR005693>, 2008.

Ewen, J., Parkin, G., and O’Connell, P. E.: SHETRAN: Distributed River Basin Flow and Transport Modeling System, *J. Hydrol. Eng.*, 5, 250–258, [https://doi.org/10.1061/\(ASCE\)1084-0699\(2000\)5:3\(250\)](https://doi.org/10.1061/(ASCE)1084-0699(2000)5:3(250)), 2000.

1085 Fan, Y., Li, H., and Miguez-Macho, G.: Global Patterns of Groundwater Table Depth, *Science*, 339, 940–943, <https://doi.org/10.1126/science.1229881>, 2013.

Franz, T. E., Zreda, M., Ferre, T. P. A., Rosolem, R., Zweck, C., Stillman, S., Zeng, X., and Shuttleworth, W. J.: Measurement depth of the cosmic ray soil moisture probe affected by hydrogen from various sources, *Water Resour. Res.*, 48, <https://doi.org/10.1029/2012WR011871>, 2012.

1090 Franz, T. E., Zreda, M., Rosolem, R., and Ferre, T. P. A.: A universal calibration function for determination of soil moisture with cosmic-ray neutrons, *Hydrol. Earth Syst. Sci.*, 17, 453–460, <https://doi.org/10.5194/hess-17-453-2013>, 2013.

Giordano, M.: Global Groundwater? Issues and Solutions, *Annu. Rev. Environ. Resour.*, 34, 153–178, <https://doi.org/10.1146/annurev.environ.030308.100251>, 2009.

1095 Goodrich, D. C., Lane, L. J., Shillito, R. M., Miller, S. N., Syed, K. H., and Woolhiser, D. A.: Linearity of basin response as a function of scale in a semiarid watershed, *Water Resour. Res.*, 33, 2951–2965, <https://doi.org/10.1029/97WR01422>, 1997.

Goodrich, D. C., Keefer, T. O., Unkrich, C. L., Nichols, M. H., Osborn, H. B., Stone, J. J., and Smith, J. R.: Long-term precipitation database, Walnut Gulch Experimental Watershed, Arizona, United States, *Water Resour. Res.*, 44, <https://doi.org/10.1029/2006WR005782>, 2008.

1100 Goodrich, D. C., Williams, D. G., Unkrich, C. L., Hogan, J. F., Scott, R. L., Hultine, K. R., Pool, D., Goes, A. L., and Miller, S.: Comparison of Methods to Estimate Ephemeral Channel Recharge, Walnut Gulch, San Pedro River Basin, Arizona, in: *Groundwater Recharge in a Desert Environment: The Southwestern United States*, American Geophysical Union (AGU), 77–99, <https://doi.org/10.1029/009WSA06>, 2013.

1105 Goodrich, D. C., Kepner, W. G., Levick, L. R., and Wigington, P. J.: Southwestern Intermittent and Ephemeral Stream Connectivity, *JAWRA J. Am. Water Resour. Assoc.*, 54, 400–422, <https://doi.org/10.1111/1752-1688.12636>, 2018.

de Graaf, I. E. M., Sutanudjaja, E. H., van Beek, L. P. H., and Bierkens, M. F. P.: A high-resolution global-scale groundwater model, *Hydrol Earth Syst Sci*, 19, 823–837, <https://doi.org/10.5194/hess-19-823-2015>, 2015.

1110 Harbaugh, A. W.: MODFLOW-2005, The U.S. Geological Survey Modular Ground-Water Model—the Ground-Water Flow Process, U.S. Geological Survey Techniques and Methods 6- A16, 2005.

Harbaugh, A. W., Banta, E. R., Hill, M. C., and McDonald, M. G.: MODFLOW-2000, The U.S. Geological Survey Modular Ground-Water Model - User Guide to Modularization Concepts and the Ground-Water Flow Process, 2000.

1115 Heilman, P., Nichols, M. H., Goodrich, D. C., Miller, S. N., and Guertin, D. P.: Geographic information systems database, Walnut Gulch Experimental Watershed, Arizona, United States, *Water Resour. Res.*, 44, <https://doi.org/10.1029/2006WR005777>, 2008.

1120 Hersbach, H., Bell, B., Berrisford, P., Hirahara, S., Horányi, A., Muñoz-Sabater, J., Nicolas, J., Peubey, C., Radu, R., Schepers, D., Simmons, A., Soci, C., Abdalla, S., Abellán, X., Balsamo, G., Bechtold, P., Biavati, G., Bidlot, J., Bonavita, M., Chiara, G. D., Dahlgren, P., Dee, D., Diamantakis, M., Dragani, R., Flemming, J., Forbes, R., Fuentes, M., Geer, A., Haimberger, L., Healy, S., Hogan, R. J., Hólm, E., Janisková, M., Keeley, S., Laloyaux, P., Lopez, P., Lupu, C., Radnoti, G., Rosnay, P. de, Rozum, I., Vamborg, F., Villaume, S., and Thépaut, J.-N.: The ERA5 global reanalysis, *Q. J. R. Meteorol. Soc.*, n/a, 1–51, <https://doi.org/10.1002/qj.3803>, 2020.

1125 Hidroinnova: Cosmic-ray soil moisture/snow sensing system user's guide, 2013.

Hobley, D. E. J., Adams, J. M., Nudurupati, S. S., Hutton, E. W. H., Gasparini, N. M., Istanbulluoglu, E., and Tucker, G. E.: Creative computing with Landlab: an open-source toolkit for building, coupling, and exploring two-dimensional numerical models of Earth-surface dynamics, *Earth Surf. Dyn.*, 5, 21–46, <https://doi.org/10.5194/esurf-5-21-2017>, 2017a.

1130 Hobley, D. E. J., Adams, J. M., Siddhartha Nudurupati, S., Hutton, E. W. H., Gasparini, N. M., Istanbulluoglu, E., and Tucker, G. E.: Creative computing with Landlab: an open-source toolkit for building, coupling, and exploring two-dimensional numerical models of Earth-surface dynamics, *Earth Surf. Dyn.*, 5, 21–46, <https://doi.org/10.5194/esurf-5-21-2017>, 2017b.

1135 Holtan, H. N.: Time-condensation in hydrograph-analysis, *Eos Trans. Am. Geophys. Union*, 26, 407–413, <https://doi.org/10.1029/TR026i003p00407>, 1945.

Huang, J., Yu, H., Guan, X., Wang, G., and Guo, R.: Accelerated dryland expansion under climate change, *Nat. Clim. Change*, 6, nclimate2837, <https://doi.org/10.1038/nclimate2837>, 2015.

1140 Huang, J., Li, Y., Fu, C., Chen, F., Fu, Q., Dai, A., Shinoda, M., Ma, Z., Guo, W., Li, Z., Zhang, L., Liu, Y., Yu, H., He, Y., Xie, Y., Guan, X., Ji, M., Lin, L., Wang, S., Yan, H., and Wang, G.: Dryland climate change: Recent progress and challenges, *Rev. Geophys.*, 55, 719–778, <https://doi.org/10.1002/2016RG000550>, 2017.

Hughes, A., Mansour, M., Robins, N., and Peach, D.: Numerical Modelling of Run-off Recharge in a Catchment in the West Bank, MODFLOW More 2006 Manag. Ground-Water Syst. Conf. Proc., 1, 385–389, 2006.

1145 Hughes, D. A.: A simple approach to estimating channel transmission losses in large South African river basins, *J. Hydrol. Reg. Stud.*, 25, 100619, <https://doi.org/10.1016/j.ejrh.2019.100619>, 2019.

IAEA: Cosmic Ray Neutron Sensing: Use, Calibration and Validation for Soil Moisture Estimation, INTERNATIONAL ATOMIC ENERGY AGENCY, Vienna, 2017.

1150 Ivanov, V. Y., Vivoni, E. R., Bras, R. L., and Entekhabi, D.: Catchment hydrologic response with a fully distributed triangulated irregular network model, *Water Resour. Res.*, 40, <https://doi.org/10.1029/2004WR003218>, 2004.

Kampf, S. K. and Burges, S. J.: A framework for classifying and comparing distributed hillslope and catchment hydrologic models, *Water Resour. Res.*, 43, <https://doi.org/10.1029/2006WR005370>, 2007.

1155 Keefer, T. O., Moran, M. S., and Paige, G. B.: Long-term meteorological and soil hydrology database, Walnut Gulch Experimental Watershed, Arizona, United States, *Water Resour. Res.*, 44, <https://doi.org/10.1029/2006WR005702>, 2008.

Kipkemoi, I., Michaelides, K., Rosolem, R., and Singer, M. B.: Climatic expression of rainfall on soil moisture dynamics in drylands, *Hydrol. Earth Syst. Sci. Discuss.*, 1–24, <https://doi.org/10.5194/hess-2021-48>, 2021.

1160 Lahmers, T. M., Gupta, H., Castro, C. L., Gochis, D. J., Yates, D., Dugger, A., Goodrich, D., and Hazenberg, P.: Enhancing the Structure of the WRF-Hydro Hydrologic Model for Semiarid Environments, *J. Hydrometeorol.*, 20, 691–714, <https://doi.org/10.1175/JHM-D-18-0064.1>, 2019.

1165 Marçais, J., de Dreuzy, J.-R., and Erhel, J.: Dynamic coupling of subsurface and seepage flows solved within a regularized partition formulation, *Adv. Water Resour.*, 109, 94–105, <https://doi.org/10.1016/j.advwatres.2017.09.008>, 2017.

Maxwell, R. M. and Condon, L. E.: Connections between groundwater flow and transpiration partitioning, *Science*, 353, 377–380, <https://doi.org/10.1126/science.aaf7891>, 2016.

1170 Mayes, M., Caylor, K. K., Singer, M. B., Stella, J. C., Roberts, D., and Nagler, P.: Climate sensitivity of water use by riparian woodlands at landscape scales, *Hydrol. Process.*, 34, 4884–4903, <https://doi.org/10.1002/hyp.13942>, 2020.

Mein, R. G. and Larson, C. L.: Modeling infiltration during a steady rain, *Water Resour. Res.*, 9, 384–394, <https://doi.org/10.1029/WR009i002p00384>, 1973.

1175 Michaelides, K. and Wainwright, J.: Modelling the effects of hillslope–channel coupling on catchment hydrological response, *Earth Surf. Process. Landf.*, 27, 1441–1457, <https://doi.org/10.1002/esp.440>, 2002.

Michaelides, K. and Wilson, M. D.: Uncertainty in predicted runoff due to patterns of spatially variable infiltration, *Water Resour. Res.*, 43, <https://doi.org/10.1029/2006WR005039>, 2007.

1180 Michaelides, K., Hollings, R., Singer, M. B., Nichols, M. H., and Nearing, M. A.: Spatial and temporal analysis of hillslope–channel coupling and implications for the longitudinal profile in a dryland basin, *Earth Surf. Process. Landf.*, 43, 1608–1621, <https://doi.org/10.1002/esp.4340>, 2018.

Miller, S. N., Youberg, A., Guertin, D. P., and Goodrich, D. C.: Channel morphology investigations using Geographic Information Systems and field research, Ffolliott Peter F Bak. Jr Malchus B Edminster Carlet. B Dillon Madelyn C Mora Karen Tech Coords Land Steward. 21st Century Contrib. Watershed

1185 Manag. 2000 March 13-16 Tucson AZ Proc RMRS-P-13 Fort Collins CO US Dep. Agric. For. Serv. Rocky Mt. Res. Stn. P 415-419, 13, 415–419, 2000.

1190 Mudd, S. M.: Investigation of the hydrodynamics of flash floods in ephemeral channels: Scaling analysis and simulation using a shock-capturing flow model incorporating the effects of transmission losses, *J. Hydrol.*, 324, 65–79, <https://doi.org/10.1016/j.jhydrol.2005.09.012>, 2006.

1195 Nash, I. E. and Sutcliffe, I. V.: River flow forecasting through conceptual models, *J. Hydrol.*, 10, 282–290, 1970.

1200 Noorduijn, S. L., Shanafield, M., Trigg, M. A., Harrington, G. A., Cook, P. G., and Peeters, L.: Estimating seepage flux from ephemeral stream channels using surface water and groundwater level data, *Water Resour. Res.*, 50, 1474–1489, <https://doi.org/10.1002/2012WR013424>, 2014.

Philip, J. R.: THE THEORY OF INFILTRATION: 1. THE INFILTRATION EQUATION AND ITS SOLUTION., *Soil Sci.*, 83, 345, 1957.

Pilgrim, D. H., Chapman, T. G., and Doran, D. G.: Problems of rainfall-runoff modelling in arid and semiarid regions, *Hydrol. Sci. J.*, 33, 379–400, <https://doi.org/10.1080/0262668809491261>, 1988.

1205 Power, D., Rico-Ramirez, M. A., Desilets, S., Desilets, D., and Rosolem, R.: Cosmic-Ray neutron Sensor PYthon tool (crspy): An open-source tool for the processing of cosmic-ray neutron and soil moisture data., *Geosci. Model Dev.*, 2021.

Quichimbo, E. A., Singer, M. B., and Cuthbert, M. O.: Characterising groundwater–surface water interactions in idealised ephemeral stream systems, *Hydrol. Process.*, 34, 3792–3806, <https://doi.org/10.1002/hyp.13847>, 2020.

1210 Rahman, M., Rosolem, R., Kollet, S. J., and Wagener, T.: Towards a computationally efficient free-surface groundwater flow boundary condition for large-scale hydrological modelling, *Adv. Water Resour.*, 123, 225–233, <https://doi.org/10.1016/j.advwatres.2018.11.015>, 2019.

Rawls, W. J., Brakensiek, D. L., and Saxton, K. E.: Estimation of Soil Water Properties, *Trans. ASAE*, 25, 1316–1320, <https://doi.org/10.13031/2013.33720>, 1982.

1215 Reinecke, R., Foglia, L., Mehl, S., Trautmann, T., Cáceres, D., and Döll, P.: Challenges in developing a global gradient-based groundwater model (G³M v1.0) for the integration into a global hydrological model, *Geosci. Model Dev.*, 12, 2401–2418, <https://doi.org/10.5194/gmd-12-2401-2019>, 2019.

1220 Renard, K. G.: The Hydrology of Semiarid Rangeland Watersheds, Agricultural Research Service, United States Department of Agriculture, 28 pp., 1970.

1225 Renard, K. G., Nichols, M. H., Woolhiser, D. A., and Osborn, H. B.: A brief background on the U.S. Department of Agriculture Agricultural Research Service Walnut Gulch Experimental Watershed, *Water Resour. Res.*, 44, <https://doi.org/10.1029/2006WR005691>, 2008.

Reynolds, J. F., Smith, D. M. S., Lambin, E. F., Turner, B. L., Mortimore, M., Batterbury, S. P. J., Downing, T. E., Dowlatabadi, H., Fernández, R. J., Herrick, J. E., Huber-Sannwald, E., Jiang, H., Leemans, R., Lynam, T., Maestre, F. T., Ayarza, M., and Walker, B.: Global Desertification: Building a Science for Dryland Development, *Science*, 316, 847–851, <https://doi.org/10.1126/science.1131634>, 2007.

Richardson, A. D., Hollinger, D. Y., Burba, G. G., Davis, K. J., Flanagan, L. B., Katul, G. G., William Munger, J., Ricciuto, D. M., Stoy, P. C., Suyker, A. E., Verma, S. B., and Wofsy, S. C.: A multi-site analysis of random error in tower-based measurements of carbon and energy fluxes, *Agric. For. Meteorol.*, 136, 1–18, <https://doi.org/10.1016/j.agrformet.2006.01.007>, 2006.

1225 Rosolem, R., Shuttleworth, W. J., Zreda, M., Franz, T. E., Zeng, X., and Kurc, S. A.: The Effect of Atmospheric Water Vapor on Neutron Count in the Cosmic-Ray Soil Moisture Observing System, *J. Hydrometeorol.*, 14, 1659–1671, <https://doi.org/10.1175/JHM-D-12-0120.1>, 2013.

1230 Schaake, J. C., Koren, V. I., Duan, Q.-Y., Mitchell, K., and Chen, F.: Simple water balance model for estimating runoff at different spatial and temporal scales, *J. Geophys. Res. Atmospheres*, 101, 7461–7475, <https://doi.org/10.1029/95JD02892>, 1996.

1235 Schmidt, A., Hanson, C., Chan, W. S., and Law, B. E.: Empirical assessment of uncertainties of meteorological parameters and turbulent fluxes in the AmeriFlux network, *J. Geophys. Res. Biogeosciences*, 117, <https://doi.org/10.1029/2012JG002100>, 2012.

1240 Schreiner-McGraw, A., Ajami, H., and Vivoni, E. R.: Extreme weather events and transmission losses in arid streams, *Environ. Res. Lett.*, <https://doi.org/10.1088/1748-9326/ab2949>, 2019.

1245 Scoging, H. M. and Thornes, J. B.: Infiltration characteristics in a semiarid environment, *Proc. Hydrol. Areas Low Precip.*, 1979.

1250 Scott, R. L., Biederman, J. A., Hamerlynck, E. P., and Barron-Gafford, G. A.: The carbon balance pivot point of southwestern U.S. semiarid ecosystems: Insights from the 21st century drought, *J. Geophys. Res. Biogeosciences*, 120, 2612–2624, <https://doi.org/10.1002/2015JG003181>, 2015.

1255 Shanafield, M., Niswonger, R. G., Prudic, D. E., Pohll, G., Susfalk, R., and Panday, S.: A method for estimating spatially variable seepage and hydraulic conductivity in channels with very mild slopes, *Hydrol. Process.*, 28, 51–61, <https://doi.org/10.1002/hyp.9545>, 2014.

1260 Sherman, L. K.: Comparison f-curves derived by the methods of sharp and Holtan and of Sherman and Mayer, *Eos Trans. Am. Geophys. Union*, 24, 465–467, <https://doi.org/10.1029/TR024i002p00465>, 1943.

1265 Siebert, S., Burke, J., Faures, J. M., Frenken, K., Hoogeveen, J., Döll, P., and Portmann, F. T.: Groundwater use for irrigation – a global inventory, *Hydrol. Earth Syst. Sci.*, 14, 1863–1880, <https://doi.org/10.5194/hess-14-1863-2010>, 2010.

1270 Šimůnek, J., Van Genuchten, M. T., and Šejna, M.: The HYDRUS software package for simulating two- and three-dimensional movement of water, heat, and multiple solutes in variably-saturated media, *Tech. Man. Version*, 1, 241, 2006.

1275 Singer, M. B. and Michaelides, K.: How is topographic simplicity maintained in ephemeral dryland channels?, *Geology*, 42, 1091–1094, <https://doi.org/10.1130/G36267.1>, 2014.

1280 Singer, M. B. and Michaelides, K.: Deciphering the expression of climate change within the Lower Colorado River basin by stochastic simulation of convective rainfall, *Environ. Res. Lett.*, 12, 104011, <https://doi.org/10.1088/1748-9326/aa8e50>, 2017.

1285 Singer, M. B., Michaelides, K., and Hobley, D. E. J.: STORM 1.0: a simple, flexible, and parsimonious stochastic rainfall generator for simulating climate and climate change, *Geosci. Model Dev.*, 11, 3713–3726, <https://doi.org/10.5194/gmd-11-3713-2018>, 2018.

1290 Singer, M. B., Asfaw, D. T., Rosolem, R., Cuthbert, M. O., Miralles, D. G., MacLeod, D., Quichimbo, E. A., and Michaelides, K.: Hourly potential evapotranspiration at 0.1° resolution for the global land surface from 1981–present, *Sci. Data*, 8, 224, <https://doi.org/10.1038/s41597-021-01003-9>, 2021.

1295 Sivapalan, M. and Milly, P. C. D.: On the relationship between the time condensation approximation and the flux concentration relation, *J. Hydrol.*, 105, 357–367, [https://doi.org/10.1016/0022-1694\(89\)90113-3](https://doi.org/10.1016/0022-1694(89)90113-3), 1989.

1300 Stone, J. J., Nichols, M. H., Goodrich, D. C., and Buono, J.: Long-term runoff database, Walnut Gulch Experimental Watershed, Arizona, United States, *Water Resour. Res.*, 44, <https://doi.org/10.1029/2006WR005733>, 2008.

1270 Tarek, M., Brissette, F. P., and Arsenault, R.: Evaluation of the ERA5 reanalysis as a potential reference dataset for hydrological modelling over North America, *Hydrol. Earth Syst. Sci.*, 24, 2527–2544, <https://doi.org/10.5194/hess-24-2527-2020>, 2020.

1275 Taylor, R. G., Scanlon, B., Döll, P., Rodell, M., Beek, R. van, Wada, Y., Longuevergne, L., Leblanc, M., Famiglietti, J. S., Edmunds, M., Konikow, L., Green, T. R., Chen, J., Taniguchi, M., Bierkens, M. F. P., MacDonald, A., Fan, Y., Maxwell, R. M., Yechieli, Y., Gurdak, J. J., Allen, D. M., Shamsuddoha, M., Hiscock, K., Yeh, P. J.-F., Holman, I., and Treidel, H.: Ground water and climate change, *Nat. Clim. Change*, 3, nclimate1744, <https://doi.org/10.1038/nclimate1744>, 2012.

1280 Taylor, R. G., Todd, M. C., Kongola, L., Maurice, L., Nahozya, E., Sanga, H., and MacDonald, A. M.: Evidence of the dependence of groundwater resources on extreme rainfall in East Africa, *Nat. Clim. Change*, 3, 374–378, <https://doi.org/10.1038/nclimate1731>, 2013.

1285 Vergnes, J.-P., Decharme, B., Alkama, R., Martin, E., Habets, F., and Douville, H.: A Simple Groundwater Scheme for Hydrological and Climate Applications: Description and Offline Evaluation over France, *J. Hydrometeorol.*, 13, 1149–1171, <https://doi.org/10.1175/JHM-D-11-0149.1>, 2012.

1290 Wagner, W., Lemoine, G., and Rott, H.: A Method for Estimating Soil Moisture from ERS Scatterometer and Soil Data, *Remote Sens. Environ.*, 70, 191–207, [https://doi.org/10.1016/S0034-4257\(99\)00036-X](https://doi.org/10.1016/S0034-4257(99)00036-X), 1999.

1295 Walker, W. R.: Guidelines for designing and evaluating surface irrigation systems, *FAO Irrig. Drain. Pap.* FAO, 1989.

1299 Wang, H. F. and Anderson, M. P.: *Introduction to Groundwater Modeling: Finite Difference and Finite Element Methods*, W.H.Freeman & Co Ltd, San Francisco, 237 pp., 1982.

1300 Wang, L., Chen, W., Huang, G., and Zeng, G.: Changes of the transitional climate zone in East Asia: past and future, *Clim. Dyn.*, 49, 1463–1477, <https://doi.org/10.1007/s00382-016-3400-4>, 2017.

1305 Wheater, H., Sorooshian, S., and Sharma, K. D. (Eds.): *Hydrological Modelling in Arid and Semi-Arid Areas*, 1 edition., Cambridge University Press, Cambridge ; New York, 222 pp., 2007.

1310 White, R. P. and Nackoney, J.: *Drylands, People, and Ecosystem Goods and Services*, 2003.

1315 Wood, E. F., Lettenmaier, D. P., Liang, X., Lohmann, D., Boone, A., Chang, S., Chen, F., Dai, Y., Dickinson, R. E., Duan, Q., Ek, M., Gusev, Y. M., Habets, F., Irandejad, P., Koster, R., Mitchel, K. E., Nasonova, O. N., Noilhan, J., Schaake, J., Schlosser, A., Shao, Y., Shmakin, A. B., Verseghe, D., Warrach, K., Wetzel, P., Xue, Y., Yang, Z. L., and Zeng, Q. C.: The project for intercomparison of land-surface parameterization schemes (PILPS) phase 2(c) Red-Arkansas River basin experiment: 1. Experiment description and summary intercomparisons, *Glob. Planet. Change*, 19, 115–135, [https://doi.org/10.1016/S0921-8181\(98\)00044-7](https://doi.org/10.1016/S0921-8181(98)00044-7), 1998.

1320 Woodward, C. S. and Dawson, C. N.: Analysis of Expanded Mixed Finite Element Methods for a Nonlinear Parabolic Equation Modeling Flow into Variably Saturated Porous Media, *SIAM J. Numer. Anal. Phila.*, 37, 24, <http://dx.doi.org/10.1137/S0036142996311040>, 2000.

1325 Woolhiser, D. A.: *KINEROS, A Kinematic Runoff and Erosion Model*, Doc. Use Man., 1989.

1330 Zimmer, M. A., Kaiser, K. E., Blaszcak, J. R., Zipper, S. C., Hammond, J. C., Fritz, K. M., Costigan, K. H., Hosen, J., Godsey, S. E., Allen, G. H., Kampf, S., Burrows, R. M., Krabbenhoft, C. A., Dodds, W., Hale, R., Olden, J. D., Shanafield, M., DelVecchia, A. G., Ward, A. S., Mims, M. C., Datry, T., Bogan, M. T., Boersma, K. S., Busch, M. H., Jones, C. N., Burgin, A. J., and Allen, D. C.: Zero or not? Causes and consequences of zero-flow stream gage readings, *WIREs Water*, 7, e1436, <https://doi.org/10.1002/wat2.1436>, 2020.

1335 Zoccatelli, D., Marra, F., Armon, M., Rinat, Y., Smith, J. A., and Morin, E.: Contrasting rainfall-runoff characteristics of floods in desert and Mediterranean basins, *Hydrol. Earth Syst. Sci.*, 23, 2665–2678, <https://doi.org/10.5194/hess-23-2665-2019>, 2019.

1315 Zreda, M., Shuttleworth, W. J., Zeng, X., Zweck, C., Desilets, D., Franz, T., and Rosolem, R.: COSMOS: the
Cosmic-ray Soil Moisture Observing System, *Hydrol. Earth Syst. Sci.*, 16, 4079–4099,
<https://doi.org/10.5194/hess-16-4079-2012>, 2012.

1320

1325

1330

1335

1340

1345

Tables

1350 **Table 1.** Model parameters for different processes considered in the model, some required parameters depend on the infiltration approach ('Inf. Method'). Default values are specified in brackets. For soil hydraulic properties, default values correspond to a sandy loam soil texture (Clapp and Hornberger, 1978; Rawls et al., 1982).

Parameter	Description	Dimension	Default Values	Inf. Method
Overland flow				
k_T	Recession time for channel streamflow	[T ⁻¹]	0.083 h ⁻¹ *	-
W	Channel width	[L]	10 m	-
L_{ch}	Channel length	[L]	grid size	-
K_{ch}	Channel saturated hydraulic conductivity	[L T ⁻¹]	10.9 mm h ⁻¹	-
Unsaturated zone				
θ_{wp}	Water content at wilting point	[-]	0.07	All
θ_{fc}	Water content at field capacity	[-]	0.17	All
θ_{sat}	Saturated water content	[-]	0.41	All
ψ	Suction head	[L]	110.1 mm	All

λ	Soil pore size distribution	[-]	4.9	All
σ_y	Standard deviation of the log saturated hydraulic	[LT ⁻¹]	0.5 mm h ⁻¹	Up-GA
K_{sat}	Saturated hydraulic conductivity	[L T ⁻¹]	120.9 mm h ⁻¹	All
D	Rooting depth	[L]	800 mm	All
kdt	Schaake reference parameter	[-]	1.0	Schaake
k	Crop coefficient	[-]	1.0	-
Saturated Zone				
S_y	Specific yield	[-]	0.01	-
K_{aq}	Aquifer Saturated hydraulic conductivity	[L T ⁻¹]	1 m h ⁻¹	-
T	Aquifer Transmissivity (for constant values)	[L T ⁻¹]	60 m ² h ⁻¹	-
fd	Effective aquifer depth (for exponential function)	[L]	60 m	-
h_b	Aquifer bottom elevation	[L]	0 m	-

*Default values correspond to a flow velocity of ~1 m s⁻¹ over a 300-m straight path

1355

1360

1365

1370

Figures

1375

Figure 1. Schematic representation of **DRYP** showing a) the main hydrological processes controlling water partitioning in dryland regions; b) distributed datasets needed to derive input parameters; c) vertical and horizontal discretization and representation of topographically-driven surface runoff, vertical flow in the unsaturated zone, and hydraulic gradient driven groundwater flow in the saturated component; d) model structure and potential processes within a single grid cell for the surface component (see Sect. 2.2), unsaturated zone (see Sect. 2.3) and saturated zone (see Sect. 2.4). Arrows represent flow directions and red lines represent anthropogenic fluxes.

1380

Figure 2. Schematic illustration of the unsaturated component. The right panel represents the variation of the ratio of potential to actual evapotranspiration in relation to the water content of the soil. Please refer to Sect. 2.2 and 2.3 for a detailed explanation of the terms shown here.

1385

Figure 3. Schematic representation of a) UZ-SZ interactions: 1a) indicates no UZ-SZ interaction whereas 2a) indicates UZ-SZ interaction (soil depth, D_{root} , is reduced to D_{uz}); b) SW-GW interactions in stream cells: boundary conditions change from no-flow to head dependent flux conditions once the stream bed or ground surface is intersected by the water table. Upper part of panel b) show the numerical implementation of SW-GW interactions in a stream cell.

1395 **Figure 4.** Synthetic tilted-V catchment and flow boundary conditions specified for model simulations.

1400 **Figure 5.** Geographic location of Walnut Gulch Experimental Watershed and location of monitoring stations

1405 **Figure 6.** Temporal variation of a) precipitation (black line) and evapotranspiration (grey line), b) water content of the unsaturated zone, c) groundwater recharge, d) runoff/discharge, and e) water table elevations. Right panels represent zoomed-in sections of the shaded areas of the left panels. Solid lines represent the variation at the catchment outlet, whereas dashed lines represent the temporal variation in the stream at 4 km from the catchment outlet. For panels b-e, blue lines represent the 'infiltration-discharge' scenario, green lines represent the 'Infiltration-evapotranspiration-discharge' scenario, and red lines represent 'Infiltration-runoff-evapotranspiration-discharge' scenario.

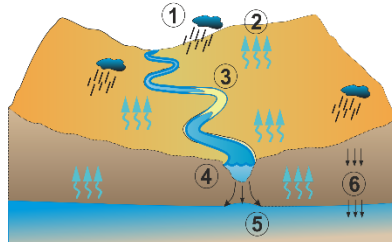
1410 **Figure 7.** Cumulative volume of main components of the water balance for the simulated scenarios: a) Infiltration – discharge, b) infiltration - evapotranspiration - discharge, and c) infiltration-infiltration excess-evapotranspiration-discharge. P is the precipitation, R is recharge, Q is discharge at the catchment outlet, AET is actual evapotranspiration, GWS is the change in groundwater storage, and Err is the water balance error of the simulation.

1415 **Figure 8.** Spatio-temporal visualisation of model process simulation at WGEW, a) rainfall event, b) soil moisture previous to the rainfall event, c) ephemeral stream for the rainfall event, and c) soil moisture after the rainfall event; x and y axes distance units are in metres.

1420 **Figure 9.** Comparison between observed and simulated values of monthly temporal variation (left) and monthly distribution (right) of a) monthly precipitation (left axes) and yearly precipitation (right axes), b) soil moisture at the COSMOS Kendall location, c) actual evapotranspiration at Kendall, d) streamflow at flume F06, e) streamflow at flume F02, and f) streamflow at flume F01. See Fig. 4 for station locations.

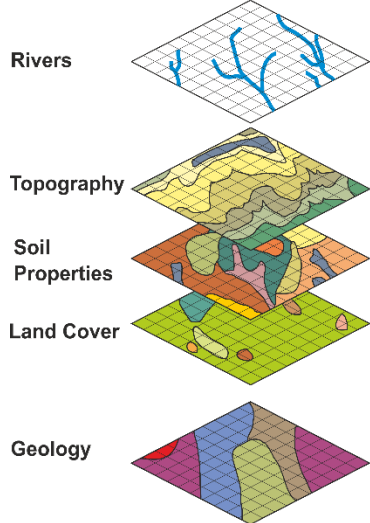
Figure 10. Average fluxes of different component of the water budget of WGEW for the simulated period, between 01/01/2007 and 01/01/2018. Blue arrows show input fluxes, green arrows represent water leaving the catchment, orange arrows represent internal surface and unsaturated zone fluxes, and yellow arrows represent water moving to the saturated zone (not modelled).

a) Main hydrological processes in drylands

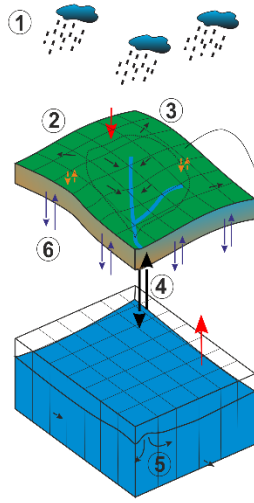


- Spatially restricted, short-lived rainstorms (1)
- High losses of precipitation by evapotranspiration (2)
- Brief and spatially variable runoff events in ephemeral drainage networks (3)
- Groundwater recharge via leaky ephemeral streams through transmission losses (4) as focussed recharge (5).
- Limited diffuse recharge (6)

b) Data



c) Spatial discretization



d) Model Cell Processes

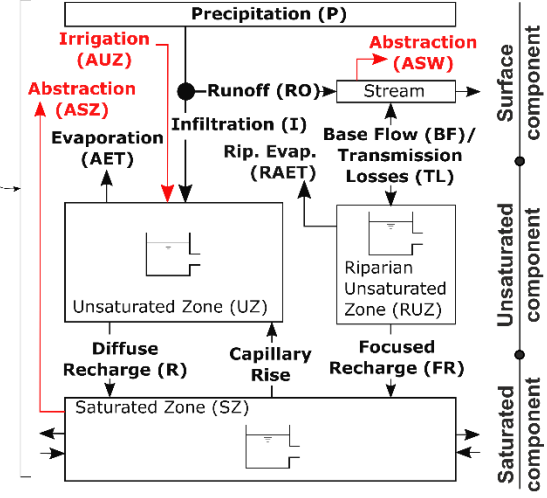


Figure 1. Schematic representation of DRYP showing a) the main hydrological processes controlling water partitioning in dryland regions; b) distributed datasets needed to derive input parameters; c) vertical and horizontal discretization and representation of topographically-driven surface runoff, vertical flow in the unsaturated zone, and hydraulic gradient driven groundwater flow in the saturated component; d) model structure and potential processes within a single grid cell for the surface component (see Sect. 2.2), unsaturated zone (see Sect. 2.3) and saturated zone (see Sect. 2.4). Arrows represent flow directions and red lines represent anthropogenic fluxes.

1425

1430

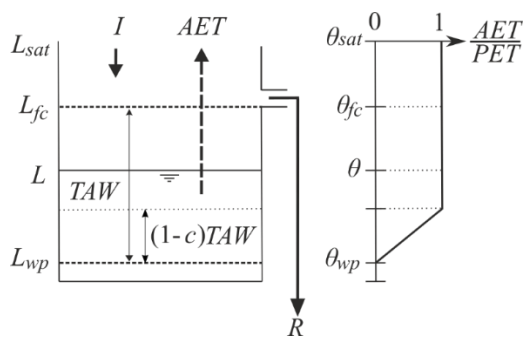
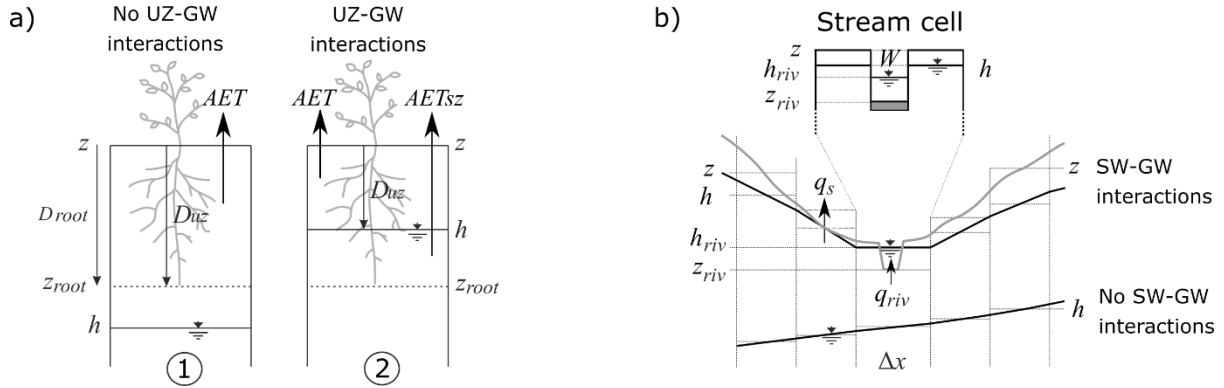
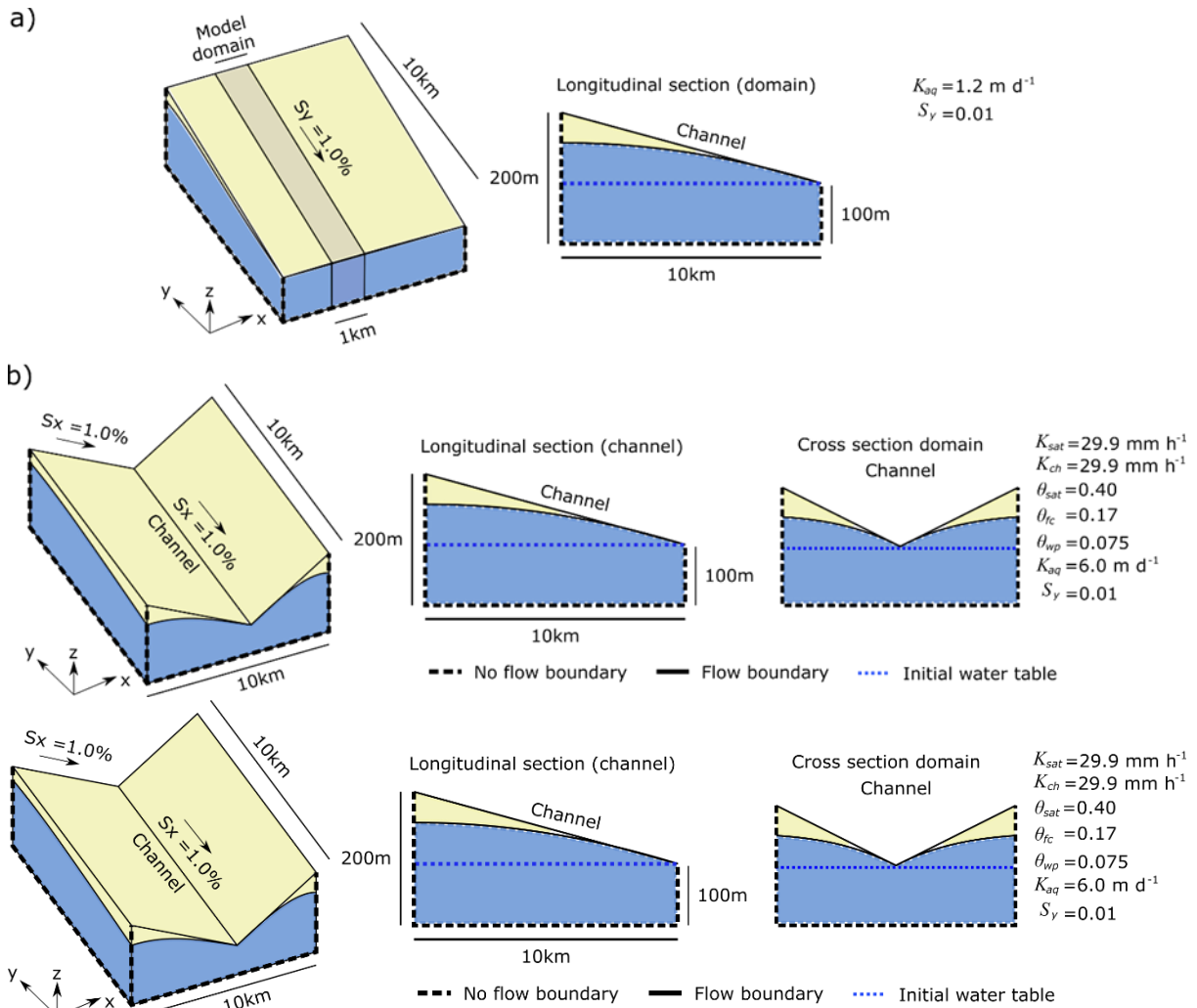


Figure 2. Schematic illustration of the unsaturated component. The right panel represents the variation of the ratio of potential to actual evapotranspiration in relation to the water content of the soil. Please refer to Sect. 2.2 and 2.3 for a detailed explanation of the terms shown here.

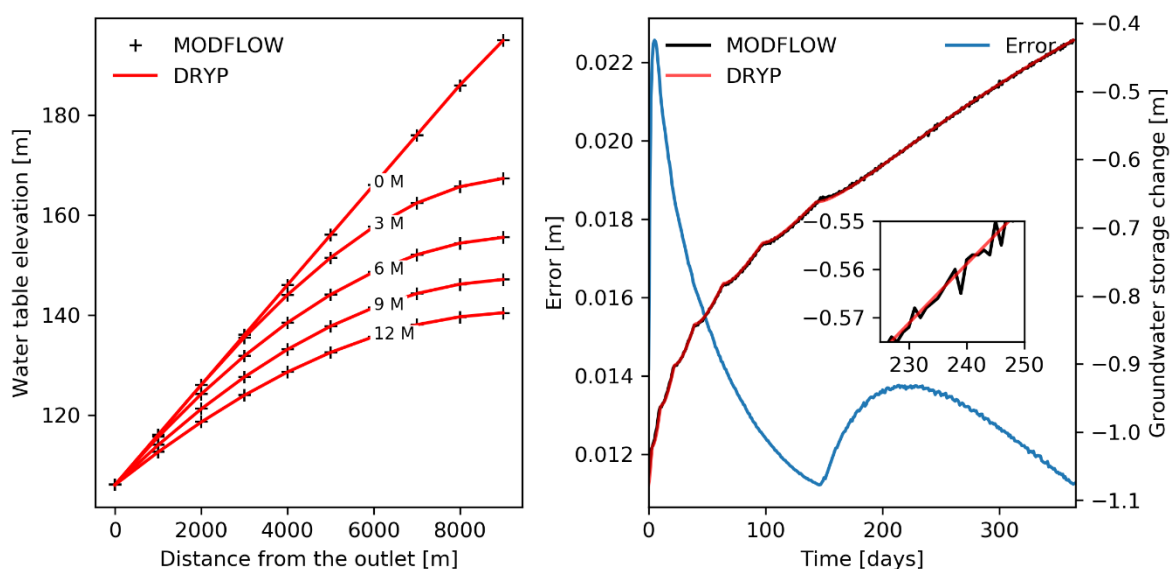
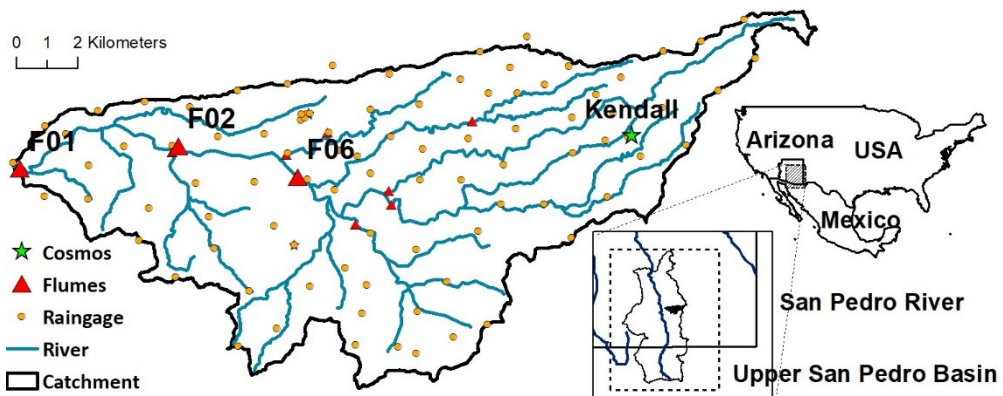
1435



1440 **Figure 3.** Schematic representation of a) UZ-SZ interactions: 1a) indicates no UZ-SZ interaction whereas 2a) indicates UZ-SZ interaction (soil depth, D_{root} , is reduced to D_{uz}); b) SW-GW interactions in stream cells: boundary conditions change from no-flow to head dependent flux conditions once the stream bed or ground surface is intersected by the water table. Upper part of panel b) show the numerical implementation of SW-GW interactions in a stream cell.



1445 **Figure 4.** Model domain for the synthetic experiments: a) 1-D model, and b) tilted-V catchment and flow boundary conditions specified for model simulations.



1455 **Figure 6.** a) Simulated head along the aquifer for different time steps (in months, M) estimated by DRYP (solid lines) and MODFLOW (dashed lines), and b) temporal variation of the mass balance error for DRYP

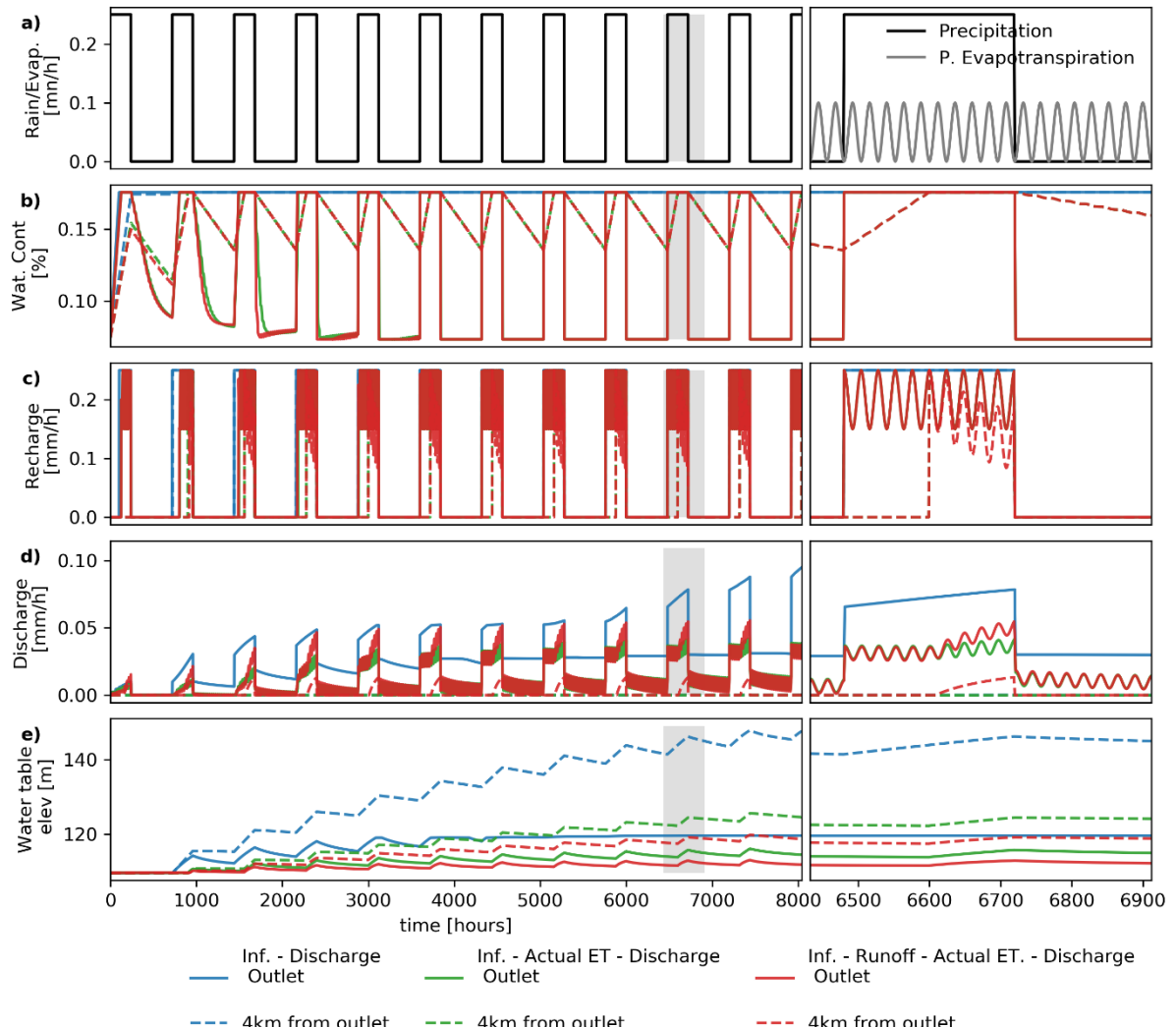
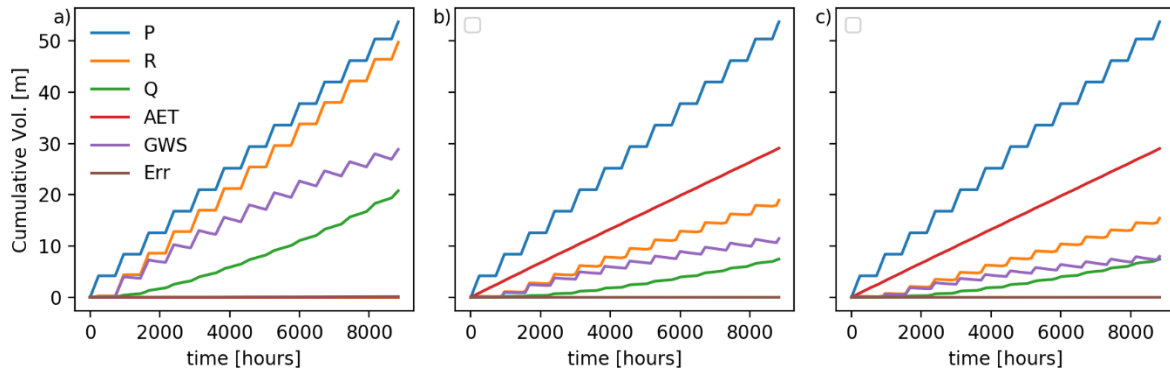


Figure 7. Temporal variation of a) precipitation (black line) and evapotranspiration (grey line), b) water content of the unsaturated zone, c) groundwater recharge, d) runoff/discharge, and e) water table elevations. Right panels represent zoomed-in sections of the shaded areas of the left panels. Solid lines represent the variation at the catchment outlet, whereas dashed lines represent the temporal variation in the stream at 4 km from the catchment outlet. For panels b-e, blue lines represent the 'infiltration-discharge' scenario, green lines represent the 'infiltration-evapotranspiration-discharge' scenario, and red lines represent 'infiltration-runoff-evapotranspiration-discharge' scenario.



1465

Figure 8. Cumulative volume of main components of the water balance for the simulated scenarios: a) Infiltration – discharge, b) infiltration - evapotranspiration - discharge, and c) infiltration-infiltration excess-evapotranspiration-discharge. P is the precipitation, R is recharge, Q is discharge at the catchment outlet, AET is actual evapotranspiration, GWS is the change in groundwater storage, and Err is the water balance error of the simulation.

1470

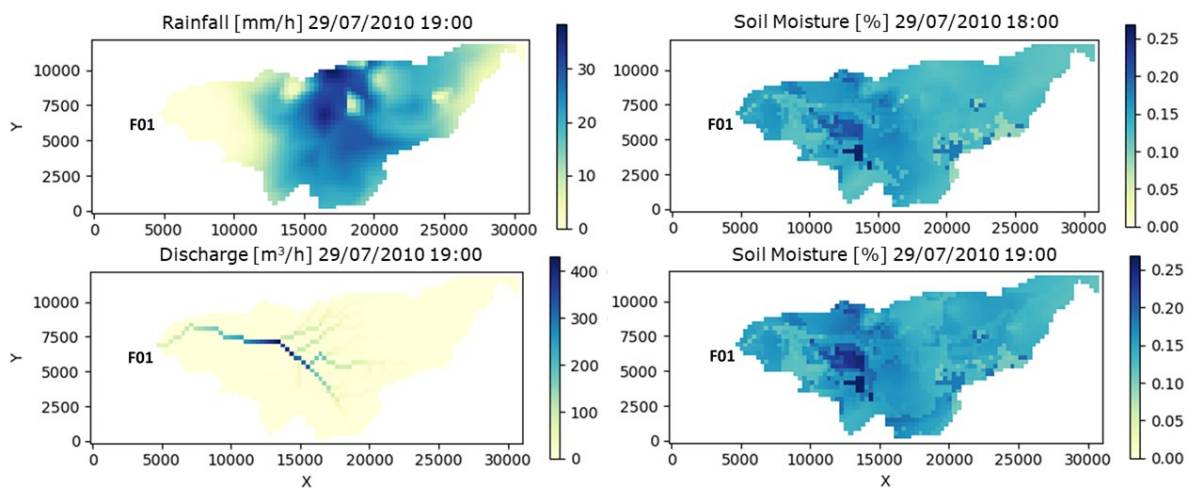


Figure 9. Spatio-temporal visualisation of model process simulation at WGEW, a) rainfall event, b) soil moisture previous to the rainfall event, c) ephemeral stream for the rainfall event, and c) soil moisture after the rainfall event; x and y axes distance units are in metres.

1475

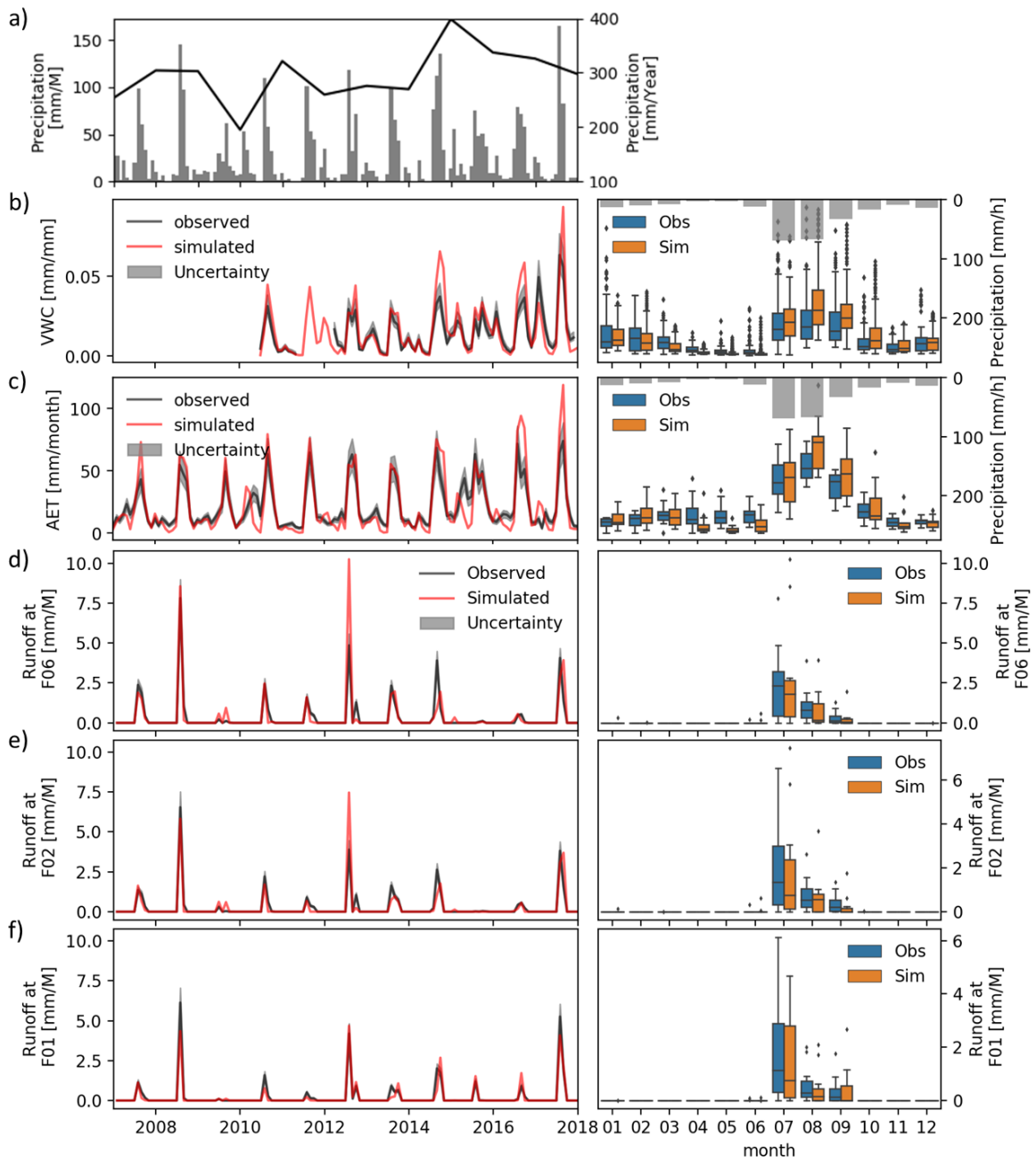


Figure 10. Comparison between observed and the best simulated run of monthly temporal variation (left) and monthly distribution (right) of a) monthly precipitation (left axes) and yearly precipitation (right axes), b) soil moisture at the COSMOS Kendall location, c) actual evapotranspiration at Kendall, d) streamflow at flume F06, e) streamflow at flume F02, and f) streamflow at flume F01. See Fig. 4 for station locations.

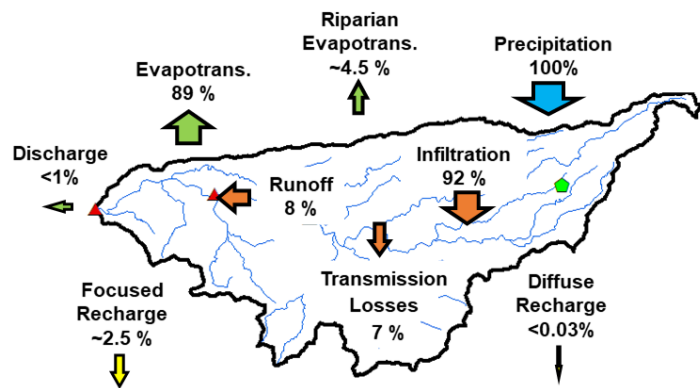


Figure 11. Average fluxes of different component of the water budget of WGEW for the simulated period, between 01/01/2007 and 01/01/2018. Blue arrows show input fluxes, green arrows represent water leaving the catchment, orange arrows represent internal surface and unsaturated zone fluxes, and yellow arrows represent water moving to the saturated zone (not modelled).